Lithos 256–257 (2016) 311–330

Contents lists available at ScienceDirect

Lithos

journal homepage: www.elsevier.com/locate/lithos

Petrogenesis of early Jurassic basalts in southern Jiangxi Province, South China: Implications for the thermal state of the Mesozoic mantle beneath South China

Tao Cen [a,b], Wu-xian Li [a,*], Xuan-ce Wang [c,d,**], Chong-jin Pang [e], Zheng-xiang Li [c,d], Guang-fu Xing [f], Xi-lin Zhao [f], Jihua Tao [g]

[a] State Key Laboratory of Isotope Geochemistry, Guangzhou Institute of Geochemistry, Chinese Academy of Science, Guangzhou 510640, China
[b] University of Chinese Academy of Sciences, Beijing 100049, China
[c] The Institute for Geoscience Research (TIGeR), Department of Applied Geology, Curtin University, Perth, WA 6845, Australia
[d] ARC Centre of Excellence for Core to Crust Fluid Systems (CCFS), Department of Applied Geology, Curtin University, Perth, WA 6845, Australia
[e] College of Earth Sciences, Guilin University of Technology, Guilin 541004, China
[f] Nanjing Institute of Geology and Mineral Resources, Nanjing 210016, China
[g] College of Earth Science, East China Institute of Technology, Nanchang 330013, China

ARTICLE INFO

Article history:
Received 17 September 2015
Accepted 30 March 2016
Available online 8 April 2016

Keywords:
Basalts
Early Jurassic
Mantle thermal state
Southern Jiangxi Province
Basin and Range-type magmatic province in South China

ABSTRACT

Early Jurassic bimodal volcanic and intrusive rocks in southern South China show distinct associations and distribution patterns in comparison with those of the Middle Jurassic and Cretaceous rocks in the area. It is widely accepted that these rocks formed in an extensional setting, although the timing of the onset and the tectonic driver for extension are debated. Here, we present systematic LA–ICP–MS zircon U–Pb ages, whole-rock geochemistry and Sr–Nd isotope data for bimodal volcanic rocks from the Changpu Formation in the Changpu–Baimianshi and Dongkeng–Linjiang basins in southern Jiangxi Province, South China. Zircon U–Pb ages indicate that the bimodal volcanic rocks erupted at ca. 190 Ma, contemporaneous with the Fankeng basalts (~183 Ma). A compilation of geochronological results demonstrates that basin-scale basaltic eruptions occurred during the Early Jurassic within a relatively short interval (<5 Ma). These Early Jurassic basalts have tholeiitic compositions and OIB-like trace element distribution patterns. Geochemical analyses show that the basalts were derived from depleted asthenospheric mantle, dominated by a volatile-free peridotite source. The calculated primary melt compositions suggest that the basalts formed at 1.9–2.1 GPa, with melting temperatures of 1378 °C–1405 °C and a mantle potential temperature (T_P) ranging from 1383 °C to 1407 °C. The temperature range is somewhat hotter than normal mid-ocean-basalt (MORB) mantle but similar to an intra-plate continental mantle setting, such as the Basin and Range Province in western North America. This study provides an important constraint on the Early Jurassic mantle thermal state beneath South China.

1. Introduction

Continental extension and rifting can cause thinning of the continental lithosphere and result in adiabatic decompressional partial melting of upwelling asthenospheric mantle (White and McKenzie, 1989; Bown and White, 1995). The generation of basalts is strongly dependent on the thermal state (including mantle potential temperature, T_P) of the upwelling mantle and the degree of lithospheric thinning (Bown and White, 1995; White and McKenzie, 1989, 1995). A relatively small increase in mantle temperature is sufficient to result in the generation of a large amount of melt under lithospheric extension; for example, an increase of temperature by 100 °C above the normal mantle temperature will double the amount of melt, whereas a 200 °C increase can quadruple it (White and McKenzie, 1989).

A prominent feature of the South China Block is that Mesozoic calc-alkaline magmatic rocks are widespread and closely associated with numerous non-ferrous and rare metal deposits (Zhou and Li, 2000; Li and Li, 2007; Z.X. Li et al., 2012). These rocks have a predominantly felsic composition and they are distributed mainly within NE-trending grabens, approximately parallel to the coastline, with an exposed area of about 218,000 km^2 (Fig. 1a; Zhou et al., 2006). Mafic members of the bimodal volcanic and intrusive rocks, previously regarded to be of Early to Middle Jurassic age, have tholeiitic compositions and intra-plate geochemical affinities. It is generally accepted that the Jurassic volcanic rocks were generated in a rift or extensional environment.

* Corresponding author.
** Correspondence to: X. Wang, The Institute for Geoscience Research (TIGeR), Department of Applied Geology, Curtin University, Perth, WA 6845, Australia.
E-mail addresses: liwx@gig.ac.cn (W. Li), x.wang3@curtin.edu.au (X. Wang).

http://dx.doi.org/10.1016/j.lithos.2016.03.022
0024-4937/

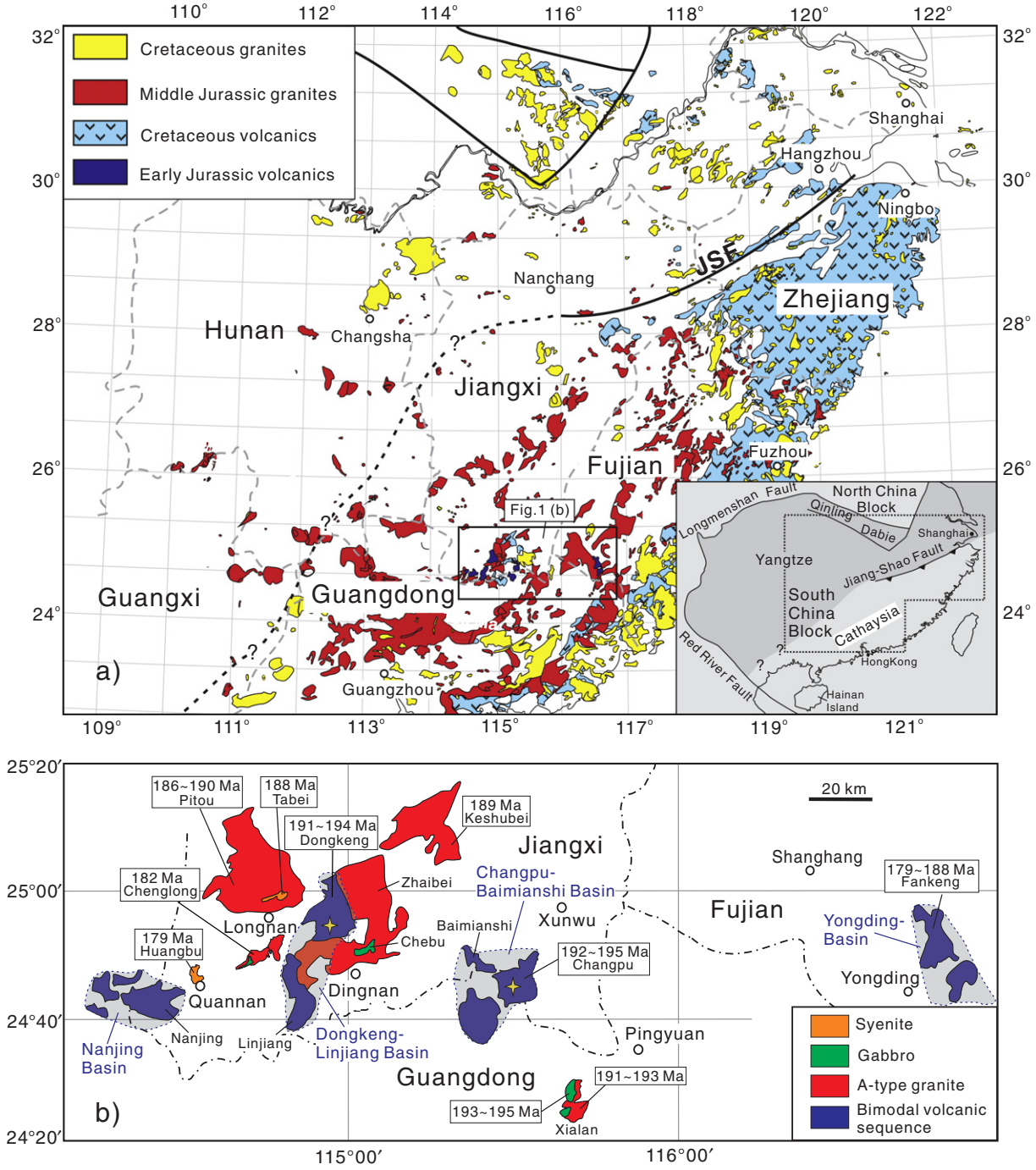

Fig. 1. (a) Distribution of the Jurassic–Cretaceous magmatic rocks in South China (modified after X.H. Li et al., 2010; Zhou et al., 2006). The inset map shows major tectonic units and location of Southeastern China. JSF: Jiangshan–Shaoxing Fault. (b) Distribution of E–W trend Early Jurassic volcanic and intrusive rocks in South China (modified after 1:200,000 geological map). Grey fields show the early Jurassic volcanic–sedimentary basins in southern Jiangxi and southwestern Fujian Provinces. Asterisks represent sample locations. Data sources: Pitou granites from Chen et al. (2004); Xialan gabbros and granites from Zhu et al. (2010); Keshubei granites from Li and Li (2007); Chenglong gabbros from He et al. (2010); Tabei synites from Chen et al. (2004); Huangbu synites from He et al. (2007); Dongkeng and Changpu bimodal volcanic rocks from Xiang and Wu (2012) and Ji and Wu (2010); Yongding bimodal volcanic rocks from Zhou et al. (2005b).

However, most continental rift-related magmas are dominantly alkalic basalts to silica-undersaturated basanites in the early phase, and the composition quickly changes to tholeiitic rocks as rifting progresses (Wilson, 1989). This does not seem to be the case for the Mesozoic basalts in South China.

In this paper, we report LA–ICP–MS zircon U–Pb ages from Mesozoic felsic volcanic rocks that are intercalated with the basaltic rocks, along with whole-rock geochemical and Sr–Nd isotopic data of the basalt samples, from the Changpu–Baimianshi and Dongkeng–Linjiang volcanic basins. Using these data, we define the timing and duration of the earliest volcanic eruptions in these basins, which possibly represent the onset of continental extension/rifting. We constrain the mantle thermal state and melting pressure using the primary basaltic melt compositions (Herzberg et al., 2007; Herzberg and Asimow, 2008; X.C. Wang et al., 2007; Wang et al., 2008, Wang et al., 2009, Wang et al., 2012). Finally, we compare

Mesozoic South China with the Basin and Range Province in western North America, and interpret the tectonic environment for Mesozoic volcanism.

2. Geological background and petrography

The South China Block (SCB) consists of the Yangtze Block to the northwest and the Cathaysia Block to the southeast, separated by the Jiangshan–Shaoxing Fault (Fig.1a, inset map; X. H. Li et al., 2012; Zhang et al., 2005). Most of the Mesozoic volcanic rocks are located within the Cathaysia Block, where granites and rhyolites are predominant and trend approximately parallel to the coastline (Fig.1a). In contrast to the felsic rocks, a suite of bimodal volcanic/intrusive rocks occur along an E–W trend between southeastern Hunan Province and southwestern Fujian Province (Fig. 1a). They are found in the Nanjing, Dongkeng–Linjiang and Changpu–Baimianshi basins in southern Jiangxi Province and the Yongding basin in southwestern Fujian Province (Fig. 1b). The best outcrops are located in the Changpu–Baimianshi and the Dongkeng–Linjiang basins. Here, the volcanic-sedimentary rocks have been named the Yutian Group, which can be divided into two formations, from bottom to top, the Shuitoujing Formation and the Changpu Formation (Fig. 2). The Shuitoujing Formation consists mainly of sandstone with conglomeratic interlayers and has a total thickness of >200 m. It unconformably overlies Paleozoic sedimentary rocks, Precambrian metamorphic rocks and Triassic granites (Dong et al., 2010; Wu et al., 2000). The overlying Changpu Formation is composed predominantly of basalt and rhyolite, along with rare pyroclastic rocks. The Changpu Formation is about 1000 m in thickness with almost equal proportions of basalt and rhyolite (Fig. 2). Coeval volcanic rocks in the Yongding basin is called the Fankeng Formation. Early geochronological studies indicated that the bimodal volcanic suites erupted between ca. 180–160 Ma, using the Rb–Sr and K–Ar whole-rock and Re–Os mineral isochron methods (Chen et al., 1999a, 1999b; Zhou et al., 2005a; Y.J. Wang et al., 2003). However, recent SHRIMP zircon U–Pb dating shows that the bimodal volcanic rocks formed at ca. 195–190 Ma (Ji and Wu, 2010; Xiang and Wu, 2012), contemporaneous with adjacent Early Jurassic A-type granites and gabbros (Fig. 1b; Chen et al., 2004; Li and Li, 2007; He et al., 2010; Zhu et al., 2010).

The basaltic rocks of the Changpu–Baimianshi and Dongkeng–Linjiang basins are mainly grey black in color, commonly with subaphyric to porphyritic texture and vesicular structure. The phenocrysts are predominantly plagioclase (5%–15%), with lesser clinopyroxene. Most plagioclase crystals are euhedral with polysynthetic twins. The matrix (85%–95%) is mainly composed of fine-grained or aphanitic clinopyroxene, plagioclase and minor Fe–Ti oxides. The rocks experienced variable degrees of alteration, showing chloritization of mafic minerals and sericitization of plagioclase.

Four rhyolite samples were collected from the Changpu Formation for U–Pb zircon dating, two of them (08GN04-1 and 08GN07-1) from the Changpu–Baimianshi basin and the other two (08GN32-1 and 08GN36-1) from the Dongkeng–Linjiang basin (Fig. 1b and Fig. 2). Ten basalts were collected from the Changpu–Baimianshi basin and thirteen were collected from the Dongkeng–Linjiang basin for geochemical analyses.

3. Analytical techniques

Zircons were separated from four rhyolitic rocks using standard density and magnetic separation techniques. Zircon grains, together with the TEMORA zircon U–Pb standard, were handpicked and mounted in an epoxy resin disk, and then polished and coated with gold. All analyzed zircon grains were documented by optical photomicrographs and cathodoluminescence (CL) images to select the best position for laser spots. Zircon U–Pb dating was conducted using laser ablation–inductively coupled plasma–mass spectrometry (LA–ICP–MS) at the State Key Laboratory of Isotope Geochemistry at the Guangzhou Institute of Geochemistry (GIG), Chinese Academy of Sciences. Helium gas was used as the carrier gas to the ICP source. NIST610 was used to optimize the instrument in order to attain the best sensitivity. TEMORA was analyzed as an external calibration standard (Black et al., 2003). Laser energy was 80 mJ and frequency was 8 Hz with ablation spots of 31 μm in diameter and 40 s ablation times. Offline selection and integration of background and analyzed signals, and time-drift correction and U–Pb dating were performed using the program ICPMSDataCal 6.7 (Liu et al., 2008). For more analytical details, see Tao et al. (2013).

Samples for geochemical analysis were crushed into small fragments (<0.5 cm in diameter) before being further cleaned and powdered in a corundum mill. Major elements were measured with a Rigaku ZSK 100e X-ray fluorescence spectrometer at the Guangzhou Institute of Geochemistry, Chinese Academy of Sciences. The analytical precision was between 1% and 5%. Loss-of-ignition (LOI) measurements were undertaken on dried sample powder by heating in a pre–ignition silica crucible to 1000 °C for 1 h and recording the weight loss. Calibration lines used to calculate major element contents of unknown samples in this study were produced by bivariate regression using 36 reference materials which cover a wide range of silicate compositions (X.H. Li et al., 2006). Trace elements were determined using a ThermoFisher X2 ICP–MS at GIG, with analytical uncertainties ranging from 1% to 5%. About 40 mg of powdered sample was dissolved in a high-pressure Teflon bomb for 48 h using a HF + HNO_3 mixture. Rh, Re and In were used as internal standards to monitor signal drift during analysis. A set of USGS standard rocks, including SY-4, AGV-2, W-2, SARM-4 and BHVO-2, were chosen as external standards for calibrating element concentrations in the measured samples. Sr and REEs were separated using cation exchange columns, followed by separation of Nd from the REE fraction using HDEHP columns. Sr and Nd isotopic analyses were carried out at GIG using a Neptune Plus (Thermo Fisher Scientific, MA, USA) multi-collection mass spectrometer equipped with nine Faraday cups and eight ion counters. The analytical procedure was similar to that of Wu et al. (2006). Measured $^{143}Nd/^{144}Nd$ ratios were normalized to $^{146}Nd/^{144}Nd = 0.7219$. The reported $^{143}Nd/^{144}Nd$ ratios were adjusted relative to the Shin Etsu JNdi-1 standard of 0.512115, corresponding to the La Jolla standard of 0.511860 (Tanaka et al., 2000).

4. Analytical results

4.1. Zircon U–Pb geochronology

The results of LA–ICP–MS zircon U–Pb dating are listed in Appendix Table 1.

Sample 08GN04-1 (24°46′53″N; 115°30′09″E) was collected from the lower part of the Changpu Formation (Fig. 2). Zircon grains were euhedral to subhedral, transparent, colorless and display magmatic growth zonation. The length of zircon grains ranges from 35 to 200 μm, with length-to-width ratios of 1.5:1 to 3:1 (Fig. 3a). Eighteen analyses were conducted on 18 zircon grains. Measured U concentrations varied from 30 to 520 ppm, and Th concentrations ranged from 54 to 415 ppm (Appendix Table 1). Th/U ratios ranged from 0.80 to 2.53, comparable to those of magmatic zircons. Four analyses (spots 5, 7, 11 and 16) generated old $^{206}Pb/^{238}U$ ages ranging from 208 to 422 Ma. These may be inherited zircon grains. Two zircon grains (spots 8 and 9) have slightly younger $^{206}Pb/^{238}U$ ages (170 and 174 Ma, respectively) due to Pb loss. The remaining 12 analyses yielded a weighted mean $^{206}Pb/^{238}U$ age of 190 ± 5 Ma (2σ, MSDW = 0.061; Fig. 3a), which is interpreted to represent the eruption age of the rhyolite.

Rhyolite sample 08GN07-1 (24°46′01″N; 115°30′31″E) was collected from the middle part of the Changpu Formation (Fig. 2). Zircon grains are mostly euhedral to subhedral, with lengths of 40 to 150 μm and length-to-width ratios of 1:1 to 3:1 (Fig. 3b). They are transparent and colorless, with oscillatory zoning visible in CL images (Fig. 3b). Twenty–five analyses were conducted on 25 grains during a single analytical session. The analyses gave variable U (89—936 ppm) and Th abundances (58–477 ppm) (Appendix Table 1), with Th/U ratios mostly

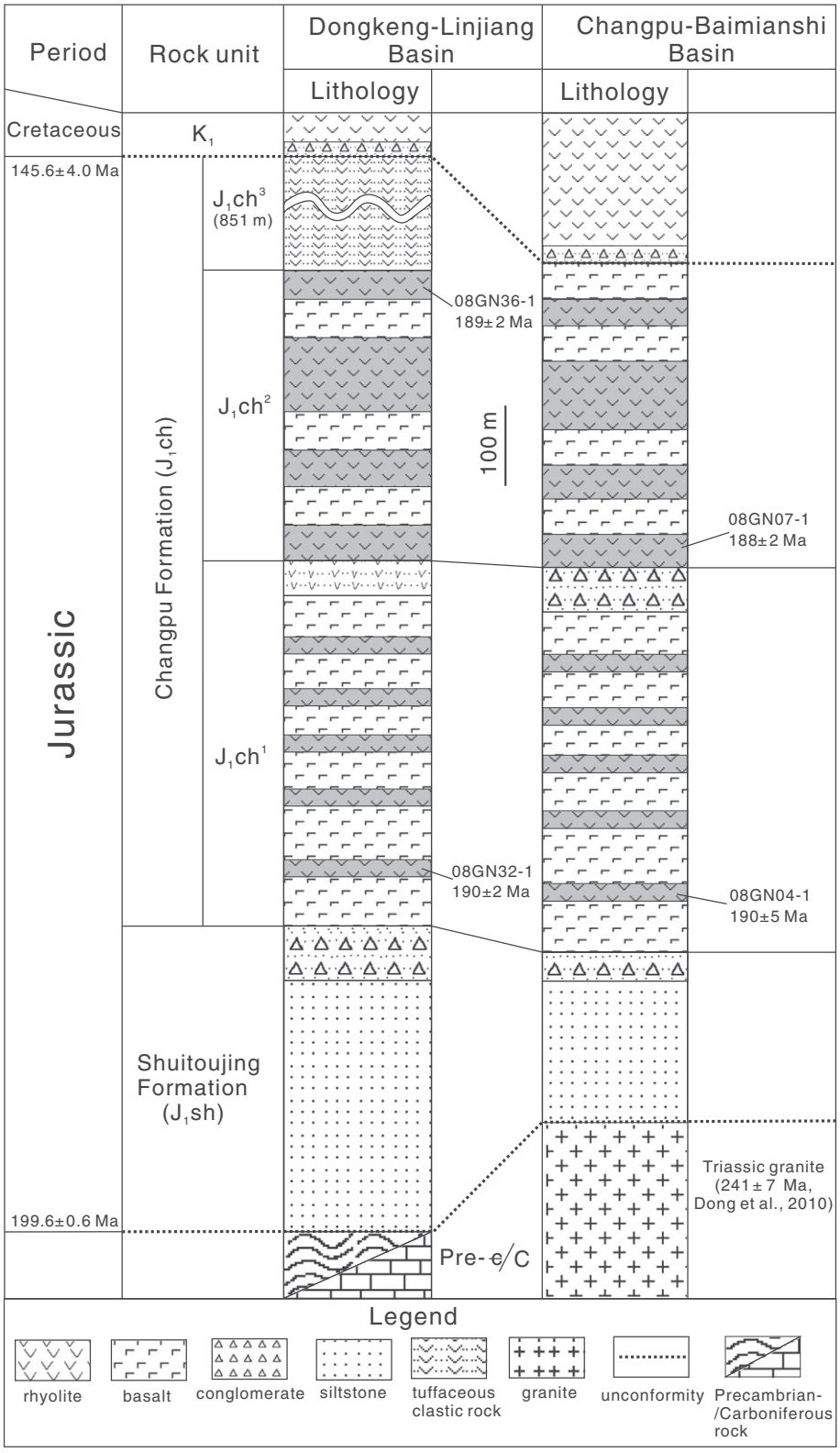

Fig. 2. Simplified stratigraphic columns of the Changpu Formation from the Dongkeng–Linjiang and Changpu–Baimianshi basins in southern Jiangxi Province (modified after Wu et al., 2000 and 1:200,000 geological map).

ranging from 0.33 to 1.18. Twenty-two of 25 analyses (excluding spots 03, 11 and 25) gave concordant results within analytical errors, producing a weighted mean $^{206}Pb/^{238}U$ age of 188 ± 2 Ma (2σ,MSWD = 1.12; Fig. 3b). This is interpreted to represent the eruption age of the rhyolite.

Rhyolite sample 08GN32-1 (24°54′01″N; 114°53′29″E) was collected from the lower part of the Changpu Formation (Fig. 2). Zircon crystals from this sample have lengths ranging from 40 to 200 μm with length-to-width ratios of 1:1 to 2:1. Most zircon grains are euhedral to

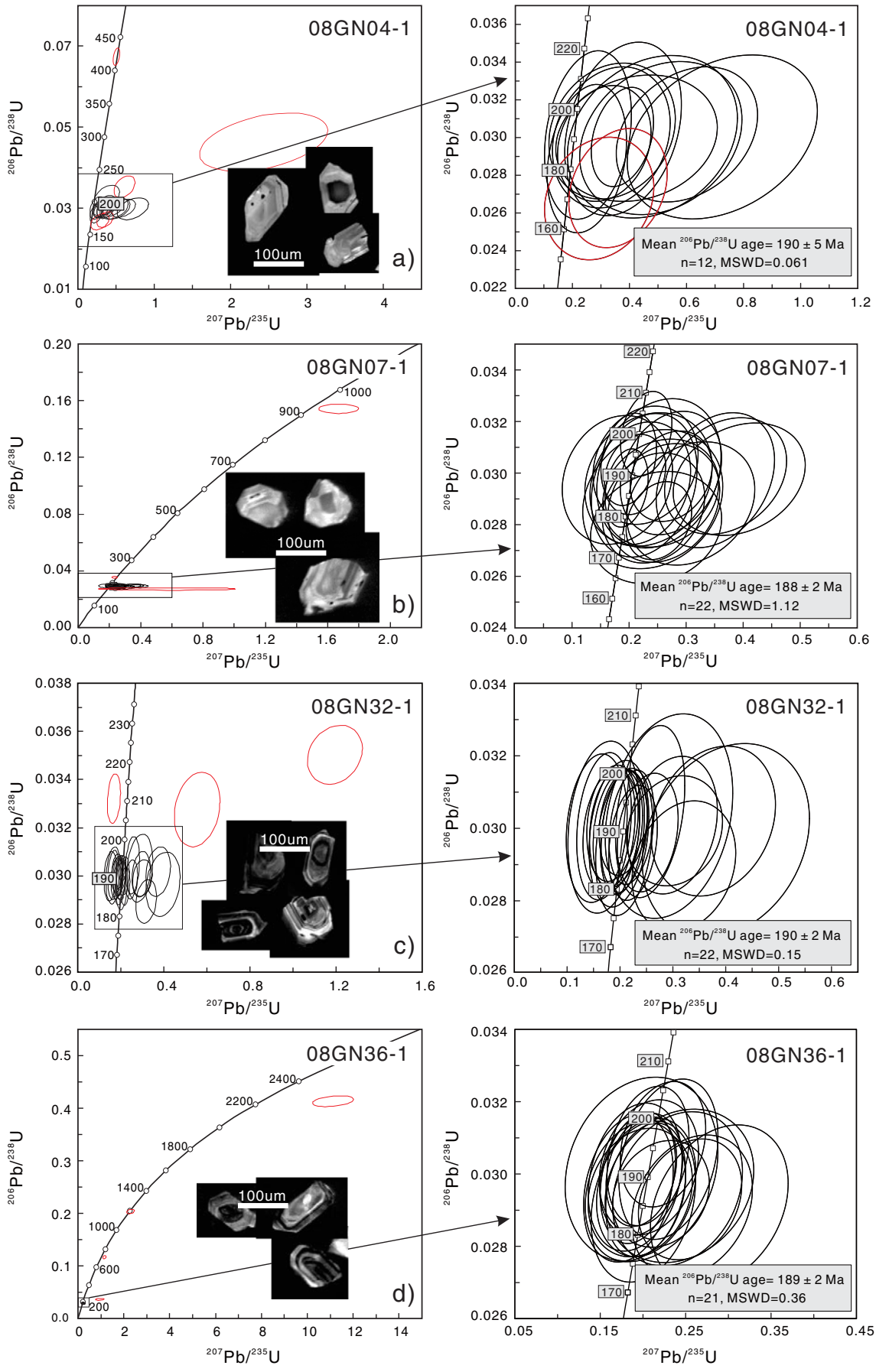

Fig. 3. LA–ICP–MS zircon U–Pb age plots and representative cathodoluminescence (CL) images of zircon grains.

Table 1
Major and trace element analytical results for the Changpu Formation basalts.

Samples	08GN05-1	08GN05-2	08GN05-3	08GN05-4	08GN05-5	08GN14-1	08GN14-2	08GN14-3	08GN14-4	08GN14-6	08GN32-7
Major elements (wt.%, normalized to 100% volatile-free)											
SiO_2	54.50	58.14	54.01	52.26	54.75	54.44	57.13	54.30	55.23	50.85	51.28
TiO_2	1.96	1.85	1.90	2.15	1.92	2.79	2.63	2.82	2.87	2.38	1.87
Al_2O_3	15.98	16.78	15.92	17.10	16.10	14.55	13.53	14.04	13.92	15.52	14.71
FeO^T	10.05	9.87	9.69	11.23	10.14	12.27	10.28	12.69	12.68	13.08	11.73
MnO	0.16	0.12	0.16	0.17	0.15	0.19	0.13	0.19	0.19	0.16	0.13
MgO	4.96	4.05	4.73	5.12	4.31	3.88	2.74	3.91	3.85	4.63	7.99
CaO	9.54	4.07	10.29	7.55	8.85	7.22	12.18	7.56	6.11	11.76	9.27
Na_2O	1.75	3.67	1.58	3.09	1.99	3.17	0.56	3.03	2.80	1.00	2.10
K_2O	0.84	1.25	1.47	1.07	1.50	1.19	0.42	1.10	2.05	0.23	0.63
P_2O_5	0.26	0.19	0.25	0.27	0.28	0.30	0.41	0.36	0.31	0.41	0.28
Total[a]	99.51	99.42	99.65	99.62	99.55	99.37	99.40	99.37	99.36	99.35	100.40
LOI	3.99	2.54	5.49	5.35	4.66	0.23	0.41	0.33	0.29	0.12	10.71
Mg#[b]	49.7	45.1	49.4	47.7	45.9	38.8	34.8	38.2	37.8	41.4	57.7
Trace elements (ppm)											
Sc	27.8	18.3	26.8	15.0	26.5	29.1	27.9	28.6	21.2	31.7	20.4
V	251	242	242	218	220	368	383	358	236	337	215
Cr	78.0	436	75.6	79.1	45.9	84.8	222	56.8	80.5	122	245
Mn	1149	858	1175	1177	1091	1480	1023	1464	1443	1215	938
Co	39.0	42.5	38.6	42.9	37.3	38.3	33.0	39.4	37.8	46.1	53.4
Ni	30.4	54.5	39.5	32.4	23.3	16.4	18.1	15.1	16.3	31.8	103
Zn	90.8	92.6	86.9	110	100	122	122	94.5	109	115	78.6
Ga	24.1	22.3	25.3	21.4	30.2	28.1	19.9	32.4	25.8	19.8	15.0
Rb	20.0	24.9	39.9	16.2	44.9	54.0	18.6	99.1	34.3	8.90	26.8
Sr	308	218	259	294	300	440	172	358	439	46	279
Y	28.3	24.6	27.7	21.0	33.8	33.9	34.1	34.5	30.9	37.3	18.3
Zr	179	164	181	176	242	250	249	250	228	222	107
Nb	13.5	12.6	13.2	10.9	18.7	17.3	18.0	18.9	18.8	17.0	12.2
Cs	1.97	1.32	1.97	0.78	2.09	4.35	1.70	6.80	3.38	1.58	2.18
Ba	346	317	412	265	555	430	77.6	670	349	39.0	75.0
La	24.7	17.5	23.3	22.5	29.1	33.8	34.1	34.2	32.5	36.8	20.9
Ce	49.5	38.0	48.5	51.4	58.1	70.2	69.3	71.1	69.4	68.8	42.9
Pr	6.58	5.07	6.49	6.16	7.65	9.40	9.20	9.50	9.06	8.96	5.75
Nd	26.5	21.2	26.5	25.2	31.1	38.0	37.8	38.6	36.8	36.5	23.5
Sm	5.91	5.04	5.79	5.41	6.86	8.16	8.05	8.26	7.83	7.60	4.84
Eu	1.74	1.50	1.71	1.76	2.13	2.31	2.23	2.31	2.21	2.15	1.49
Gd	5.80	5.05	5.69	5.31	6.89	7.81	7.80	7.87	7.57	7.65	4.43
Tb	0.93	0.86	0.92	0.86	1.10	1.21	1.20	1.23	1.17	1.18	0.67
Dy	5.46	5.28	5.40	5.09	6.52	6.84	6.83	6.94	6.64	6.86	3.67
Ho	1.10	1.07	1.09	1.04	1.31	1.35	1.34	1.36	1.31	1.37	0.71
Er	2.98	2.87	2.94	2.81	3.63	3.58	3.61	3.62	3.50	3.71	1.81
Tm	0.44	0.42	0.43	0.41	0.53	0.51	0.51	0.51	0.49	0.52	0.26
Yb	2.73	2.56	2.67	2.54	3.30	3.10	3.18	3.12	3.04	3.25	1.60
Lu	0.40	0.38	0.40	0.38	0.50	0.46	0.46	0.46	0.45	0.48	0.24
Hf	4.82	4.57	4.64	4.80	6.25	6.45	6.38	6.43	5.89	5.69	3.17
Ta	0.91	0.87	0.89	0.53	1.20	1.06	1.26	1.33	1.21	1.12	0.83
Pb	8.66	9.82	9.52	11.9	8.96	13.7	8.36	14.4	12.6	9.98	12.1
Th	5.22	2.73	5.09	3.08	4.90	9.41	9.24	9.47	7.45	6.21	3.15
U	0.73	0.52	0.70	0.74	0.75	1.22	1.17	1.22	1.21	1.61	0.68

[a] Before normalization and including loss-on-ignition (LOI).
[b] Mg# = 100*Mg/(Mg+Fe^{2+}), assuming Fe^{2+}/Fe^{total} = 0.9.

subhedral and display concentric magmatic zoning in CL images (Fig. 3c). Twenty–five analyses were conducted on 25 zircon grains. They record variable U (46–603 ppm) and Th (32–313 ppm) contents, with Th/U ratios ranging from 0.27 to 1.19 (Appendix Table 1). The analyses of 13, 15 and 19 are obvious discordant, therefore they were rejected in age calculating. The remaining twenty-two analyses gave a weighted mean $^{206}Pb/^{238}U$ age of 190 ± 2 Ma (2σ, MSWD = 0.15; Fig. 3c). This is interpreted to represent the eruption age of this rhyolite.

Rhyolite sample 08GN36-1 (24°51′31″N; 114°56′35″E) was collected from the middle part of the Changpu Formation (Fig. 2). Zircon grains are euhedral to subhedral and have lengths ranging from 20 to 100 μm, with length to width ratios between 1:1 and 2:1 (Fig. 3d). They are transparent and colorless, with euhedral concentric zoning common in most crystals in CL images. Twenty-five analyses from 25 zircons were obtained during a single analytical session. These grains have U = 86 to 312 ppm and Th = 54 to 221 ppm, with Th/U ratios ranging from 0.33 to 0.80 (Appendix Table 1). Excluding two discordant analyses (spots 14 and 23) and two inherited zircons (spots 12 and 18) which have Neoproterozoic (~720 Ma) and Mesoproterozoic (~1200 Ma) ages, twenty-one analyses yielded a weighted mean $^{206}Pb/^{2386}U$ age of 189 ± 2 Ma (2σ, MSWD = 0.36; Fig. 3d), which is interpreted as the eruption age of this rhyolite.

These results suggest that the Changpu Formation rhyolites formed during the Early Jurassic (ca. 190 Ma), contemporaneous with the adjacent Fankeng basalts in southwestern Fujian Province where intercalated rhyolites were dated as 179–188 Ma by whole-rock and mineral Rb–Sr isochrons (Xu, 1992; Zhou and Chen, 2001; Zhou et al., 2005b).

4.2. Major and trace element compositions

The results are presented in Table 1 (normalized to 100 wt.%). The samples are characterized by variable SiO_2 (Fig. 4), high TiO_2 and FeO^T, and moderate CaO and Al_2O_3 concentrations (Fig. 5a–d). Their Zr contents range from 107 to 251 ppm and on the Zr/TiO_2 versus Nb/Y diagram of Winchester and Floyd (1976), most samples plot within

08GN32-8	08GN32-9	08GN32-11	08GN32-12	08GN34-1	08GN34-2	08GN34-4	08GN45-1	08GN45-4	08GN45-5	08GN45-8	08GN45-9
47.22	46.80	53.43	46.37	52.13	52.19	51.34	54.60	52.79	53.96	49.80	47.58
2.61	4.96	2.64	5.12	3.03	3.03	2.99	2.82	3.03	2.86	3.19	3.33
16.58	15.70	15.72	15.95	15.05	14.84	15.13	14.57	15.96	14.86	14.87	15.40
9.72	15.07	10.57	14.93	13.20	13.11	13.25	12.93	14.62	13.32	13.49	13.66
0.19	0.18	0.10	0.19	0.18	0.19	0.19	0.20	0.29	0.22	0.22	0.26
3.72	5.17	6.63	5.05	4.50	4.43	4.76	4.88	5.64	5.61	5.15	5.59
13.29	6.72	5.31	6.69	9.25	9.44	9.79	6.09	5.54	6.12	9.47	10.69
3.05	1.88	3.37	2.15	1.79	1.76	1.86	3.26	1.30	2.59	2.80	2.57
3.05	2.70	1.71	2.71	0.55	0.70	0.39	0.39	0.56	0.21	0.45	0.34
0.57	0.83	0.53	0.85	0.31	0.30	0.31	0.25	0.26	0.26	0.56	0.59
100.44	99.77	99.79	99.83	99.51	99.51	99.45	99.67	99.76	99.68	99.63	99.63
11.38	6.40	6.81	6.86	3.46	3.74	3.01	1.95	3.43	2.22	0.79	0.81
43.3	40.7	55.6	40.4	40.6	40.4	41.8	43.0	43.6	45.7	43.3	45.0
23.9	19.1	22.7	18.9	27.8	28.1	28.1	31.7	33.6	32.3		21.1
296	323	273	335	349	354	358	385	471	426		344
172	29.6	212	16.1	30.2	32.5	87.1	3.62	62.9	89.0		92.2
1323	1377	750	1443	1360	1391	1448	1517	2211	1687		1994
38.7	50.7	35.8	54.0	46.0	51.8	43.3	53.5	53.5	52.9		45.4
56.4	42.0	58.2	40.7	24.0	23.9	27.6	16.5	17.8	19.0		50.7
77.9	114	90.9	112	120	122	124	109	119	117		86.9
23.5	46.5	23.4	34.7	22.5	23.8	22.6	21.2	22.1	21.4		19.0
127	99.8	85.9	116	16.2	20.0	8.27	20.1	41.1	14.4		8.94
327	343	206	350	296	306	316	481	353	419		411
24.5	24.8	23.3	24.3	34.3	34.4	34.5	32.8	32.5	33.9		33.0
159	179	155	179	241	245	246	214	226	218		252
18.2	11.4	17.7	24.1	17.9	18.0	17.9	15.3	17.3	14.7		22.3
4.55	6.87	6.22	6.53	1.04	1.62	0.72	4.97	9.27	1.86		3.11
342	1305	329	799	200	255	189	176	179	160		110
25.3	27.6	25.4	28.0	27.2	27.4	27.4	27.0	26.9	27.2		28.6
53.0	59.4	52.9	61.1	57.1	58.3	57.6	56.7	58.4	58.1		62.7
7.35	8.37	7.27	8.58	7.89	8.02	7.92	7.63	7.98	7.88		8.78
30.7	36.1	30.3	36.9	33.0	33.6	33.2	31.4	32.8	32.6		37.3
6.49	7.60	6.29	7.71	7.45	7.48	7.48	6.91	7.26	7.29		8.23
1.97	3.00	1.87	3.57	2.22	2.28	2.28	2.07	1.95	2.06		2.66
6.01	6.93	5.75	7.03	7.19	7.35	7.31	6.84	6.98	7.10		7.91
0.90	0.99	0.87	0.99	1.15	1.17	1.18	1.11	1.11	1.14		1.24
5.00	5.27	4.78	5.23	6.75	6.85	6.84	6.43	6.44	6.66		7.15
0.97	0.99	0.94	0.97	1.35	1.36	1.36	1.28	1.30	1.32		1.42
2.50	2.44	2.40	2.39	3.62	3.70	3.71	3.44	3.46	3.53		3.78
0.35	0.33	0.34	0.32	0.52	0.54	0.54	0.49	0.50	0.50		0.53
2.15	1.94	2.08	1.90	3.23	3.29	3.32	3.05	3.04	3.11		3.28
0.32	0.28	0.31	0.28	0.48	0.49	0.49	0.45	0.45	0.46		0.48
4.25	4.60	4.15	4.50	6.04	6.13	6.20	5.43	5.74	5.51		5.99
1.29	0.42	1.22	1.78	1.32	1.31	1.28	1.03	1.28	0.89		1.58
14.4	8.13	6.66	9.55	10.8	12.0	12.1	12.7	11.6	14.0		7.62
4.12	3.42	4.02	3.32	6.90	7.09	7.02	7.73	8.22	7.92		4.34
0.84	0.74	1.20	0.93	1.14	1.18	1.18	1.33	1.42	1.41		0.97

the subalkaline basalt field, with variable Nb/Y ratios (Fig. 4a). Similar results were also observed in the total alkalis versus silica (TAS) diagram (not shown). On the FeO^T/MgO versus SiO_2 diagram (Fig. 4b), all samples plot in the tholeiitic field, consistent with the AFM diagram (not shown). All samples show relatively low $Mg^{\#}$ (Table 1; Fig. 5).

The basalts are characterized by enrichment in incompatible trace elements similar to OIB (Fig. 6a), but are weakly depleted in Nb and Ta relative to La with $(Nb/La)_{PM}$ ratios of 0.4–0.83. They have low total REE contents (Table 1). On the chondrite-normalized REE diagram (Fig. 6b), most samples display slightly enriched LREE patterns. With the exception of two samples, the samples exhibit weakly positive Eu anomalies. They also have low compatible element concentrations, including Cr and Ni (Table 1).

4.3. Sr–Nd isotopes

Eight basaltic samples were selected for whole-rock Sr and Nd isotope and the results are listed in Table 2. The basalts have initial $^{87}Sr/^{86}Sr$ ratios ranging from 0.7083 to 0.7102, $^{147}Sm/^{144}Nd$ ranging from 0.1247 to 0.1439 and $^{143}Nd/^{144}Nd$ varying from 0.51231 to 0.51251, corresponding to εNd (190 Ma) values of −4.8 to −1.0.

5. Discussion

5.1. Effects of alteration on whole-rock compositions

The studied samples have a large range in LOI values (Appendix Fig. A-1), indicating that they underwent varying degrees of alteration. This is consistent with the presence chloritization and sericitization by our petrographic observation. The mobile element concentrations may have been modified during alteration (X.C. Wang et al., 2010). Therefore, prior to discussing the geochemical characteristics and petrogenesis, the effect of alteration and the mobility of major and trace elements of the samples were evaluated.

Plots of LOI versus selected major elements can be used to evaluate the effect of alteration on chemical composition (X.C. Wang et al., 2010). As shown in Appendix Fig. A-1, the samples display a positive correlation of K_2O with LOI, implying that some of the Plagioclase breakdown cause the K_2O to leach out. Other major elements show no

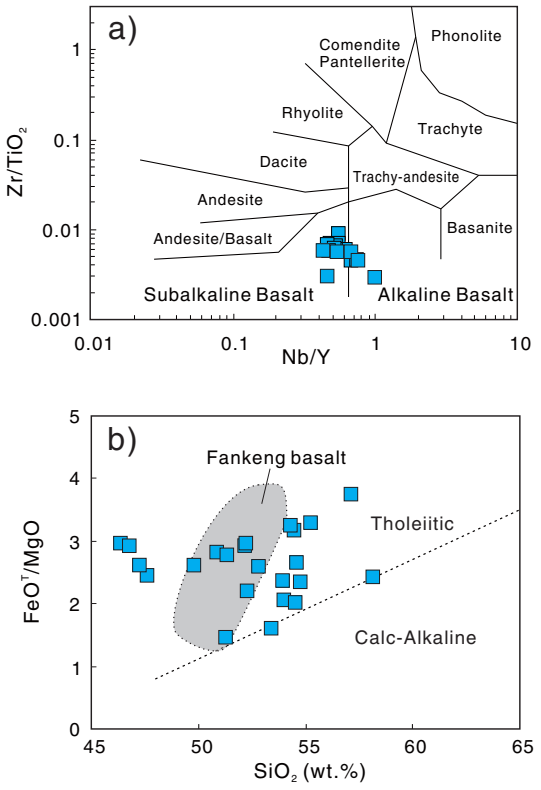

Fig. 4. (a) Zr/TiO_2 versus Nb/Y diagram (Winchester and Floyd, 1976) for the classification of the Changpu basalts. (b) Plots of FeO^T/MgO versus SiO_2 for the Changpu basalts. The shadow area outlines the composition of contemporary Fankeng basalts according to the dataset from Zhou et al. (2005b). Both the Changpu and Fankeng basalts show tholeiitic affinity in (b).

correlation with LOI values, suggesting that they were essentially immobile during alteration. Zirconium (Zr), considered to be the most immobile element during low-grade alteration of mafic to intermediate igneous rocks, can be used for the evaluation of alteration effects on the chemical composition of these rocks (e.g., Polat et al., 2002; X.C. Wang et al., 2010). We plotted TiO_2, P_2O_5, Th, Nb, Yb, Sm, La, Y, Sr, Rb, U and V against Zr to evaluate their mobility during alteration (Appendix Fig. A-2). The basalts generally show a positive correlation between Zr and high field strength elements (HFSE, such as Ti and Nb), rare earth elements (REE) and Th, suggesting that these elements were immobile during alteration. In contrast, the lack of correlations between Zr and low field strength elements (LFSE: Cs, Rb, Ba) suggests the mobility of these elements during post-magmatic alteration. The positive correlation between Sr and Zr implies that Sr is essentially immobile. In the following discussion, only the immobile elements are considered.

5.2. Effects of fractionation and crustal contamination

Primary basaltic melts should have Ni > 400 ppm, Cr > 1000 ppm and $Mg^{\#}$ between 73 and 81 (Wilson, 1989). The Changpu and Fankeng basalts have MgO between 2.74 wt.% and 8.58 wt.% and variable Ni contents between 15 and 103 ppm, indicating a highly evolved nature. Fig. 5f shows that at $Mg^{\#} > 55$, Ni decreases sharply with decreasing $Mg^{\#}$, whereas FeO^T and TiO_2 remain almost constant, reflecting olivine crystallization at $Mg^{\#} > 55$. For $Mg^{\#} < 55$, the decrease in Ni becomes slower with decreasing $Mg^{\#}$, whereas FeO^T increases rapidly at $Mg^{\#} > 40$. The presence of a positive correlation between Al_2O_3 and $Mg^{\#}$ at $Mg^{\#} < 50$ suggests that plagioclase started to crystallize at about $Mg^{\#} = 50$. Total iron contents (FeO^T) quickly depleted with decreasing of $Mg^{\#}$ at $Mg^{\#} \leq 40$. This reflects the effects of Fe-Ti oxide fractionation on whole-rock compositions at $Mg^{\#} \leq 40$. Scandium contents in the Changpu basalts increase with decreasing $Mg^{\#}$ from 50 to $Mg^{\#} > 44$ and then decrease at $Mg^{\#} < 44$ (Fig. 5e), suggesting that clinopyroxene becomes a major crystallizing phase at $Mg^{\#} \leq 44$. This is consistent with the CaO/Al_2O_3–$Mg^{\#}$ correlation where CaO/Al_2O_3 ratios sharply decrease below $Mg^{\#} \leq 44$. Because $MgO = -0.0023 \times (Mg^{\#})^2 - 0.0578(Mg^{\#}) + 2.8296$, $R^2 = 0.70$ for the Changpu basalts, the above analysis implies that for samples with > 5.7 wt.% MgO (corresponding to $Mg^{\#} = 50$), the effect of plagioclase and clinopyroxene on the whole-rock sample compositions can be ignored. The Fankeng basalts can be divided into high- (≥55) and low-$Mg^{\#}$ (≤40) sub-types (Fig. 5). The presence of an $Mg^{\#}$ gap makes it difficult to test their liquid line of descent. We therefore only examine the effect of plagioclase and clinopyroxene fractionation on whole-rock compositions. The high-$Mg^{\#}$ Fankeng basalts have nearly constant FeO^T and Eu contents and define positive correlations between CaO and $Mg^{\#}$ (Fig. 7a–c). This suggests that olivine fractionation is the controlling factor affecting their whole-rock major and trace element compositions. The contribution from plagioclase and clinopyroxene can be ignored for the high-$Mg^{\#}$ Fankeng basalts ($Mg^{\#} > 55$, corresponding to MgO > 7.5 wt.%).

The Changpu and Fankeng basalts are characterized by weakly negative Nb–Ta anomalies (Fig. 6a), variable $\varepsilon Nd(t)$ values (−4.79 to +3.55; Fig. 8e) and tight correlations between Nd isotopes and incompatible trace element ratios (Nb/La, Nb/Th, Zr/Nb and Nb/Ta). This implies that source heterogeneity and/or assimilation by lithosphere (mantle + crust) should have played an important role in their generation.

To evaluate the effect of crustal contamination, we examined correlations between selected trace element ratios including Nb/La, Nb/Th, Th/Ta and Zr/Nb. Any correlations between these ratios could be caused by crustal contamination or contributions from an enriched subcontinental lithospheric mantle (SCLM), but the latter should not produce correlations between major elements (such as MgO, SiO_2 and FeO^T), isotope ratios and the above-mentioned trace element ratios (X.C. Wang et al., 2008, 2015, 2016). Both the Changpu and Fankeng basalts exhibit clear correlations between Nb/La with Nb/Th, Th/Ta, Zr/Nb and $\varepsilon Nd(t)$ (Fig. 8a–d), likely indicating crustal contamination and/or the involvement of SCLM components. No clear correlation is found in the bivariation diagrams of Nb/U versus SiO_2/MgO and Nb/La versus MgO (figures not shown), ruling out the possibility of significant crustal contamination (e.g., X.C. Wang et al., 2008, 2014). Although the Changpu basalts display a large range of major element compositions, they have nearly constant Sm/Nd (0.20–0.22) and La/Sm ratios (mostly ranging from 3.5 to 4.2). This also argues strongly against significant crustal contamination. More importantly, although both the Changpu and Fankeng basalts display a large range of SiO_2 (46.4–57.1 wt.%), MgO (2.74–7.99 wt.%) and Al_2O_3 (13.0–17.1 wt.%) contents, they have a narrow range of Nd isotopes ($\varepsilon Nd(t) = -0.98$ to −4.79 for Changpu and −0.70 to 3.55 for Fankeng), without a correlation between $\varepsilon Nd(t)$ and SiO_2. Furthermore, the highest-silica value for Fankeng basalts has the highest $\varepsilon Nd(t)$, up to +3.55. This suggests that crustal contamination, commonly introducing a wider range of $\varepsilon Nd(t)$ values due to complex crustal compositions, was insignificant in the generation of these basalts. The maximum contribution from crustal contamination can be constrained by a mass balance calculation through mixing between two extreme end-members (MORB-like mantle and a supracrustal component, typical S-type granite here). As shown in Fig. 8f, the maximum proportion of crustal input is 10% to 20%. Considering the unradiogenic nature of the SCLM with $\varepsilon Nd(t) = -7$ to −11 (Fang et al., 2002), the actual contribution from a crustal component should be much lower than this value. Because of higher $\varepsilon Nd(t)$ values, the proportion of crustal input to the Fankeng basalts was less than for the Changpu basalts.

Due to insignificant crustal contamination, the tight correlations in Fig. 8 (a, b, c, d) therefore suggest that one end-member has high Nb/La (>0.9), $\varepsilon Nd(t)$ (≥ +3.55), Nb/Th (>8), low Zr/Nb (≤7.0) and Th/Ta (≤1.0), a typical characteristic of asthenospheric mantle-derived melts. Furthermore, SCLM-derived melts are generally unsaturated in silica, enriched in alkalis (Na + K) and incompatible trace elements (usually higher than an average value of OIBs), and

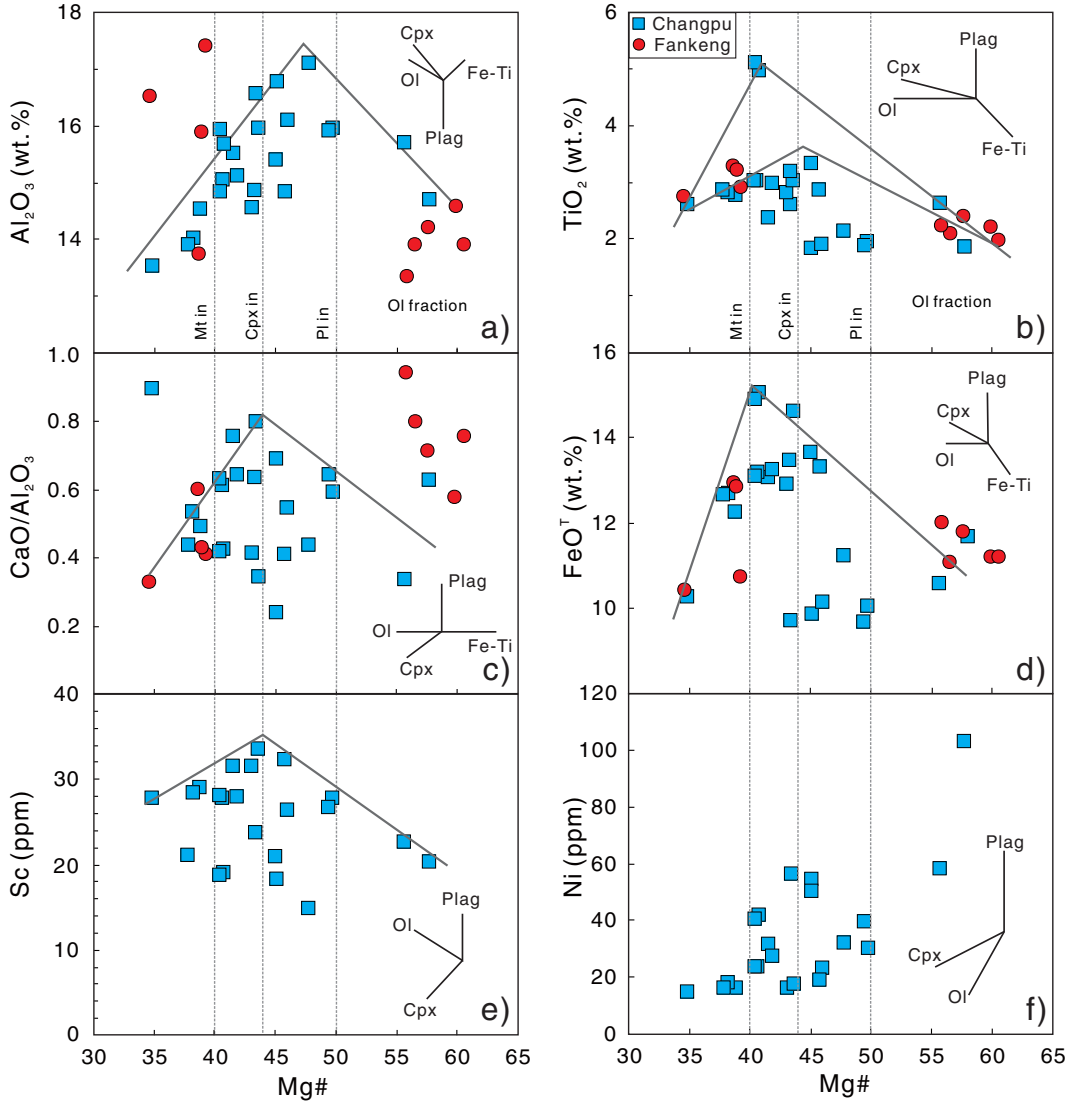

Fig. 5. Binary variation diagrams of the Changpu and Fankeng basalts showing major and trace elements variation as functions of $Mg^{\#}$. $Mg^{\#} = 100*Mg/(Mg+Fe^{2+})$, assuming $Fe^{2+}/Fe^{total} = 0.9$, cation ratio. The crystallization trend is after X.C. Wang et al. (2012).

unradiogenic Nd isotopes (X.C. Wang et al., 2008, 2009, 2014). In contrast, the Fankeng and Changpu basalts are saturated to over-saturated (19 of 23 samples with over-saturated SiO_2 >50 wt.%) silica, have a tholeiitic affinity, have relatively low incompatible trace element contents (between E-MORB and OIB; Fig. 6), and high $\varepsilon Nd(t)$ (up to +3.55). Therefore, the asthenospheric mantle should be the dominant source region of the Changpu and Fankeng basalts.

In summary, the primary magma of the Early Jurassic basalts from southern Jiangxi Province crystallized olivine at $Mg^{\#}$ >55, plagioclase at $Mg^{\#} = 50$, clinopyroxene at $Mg^{\#} = 44$ and Fe–Ti oxides at $Mg^{\#} =$ 35–40. Crustal contamination was insignificant in the generation of these basalts and the asthenospheric mantle was the dominant source.

5.3. Primary magma and melting conditions

Chemical composition of primary melts can reflect the chemical and thermal conditions of the magma source (e.g., Wang et al., 2007b, Wang et al., 2008, Wang et al., 2009, Wang et al., 2012; Herzberg et al., 2007; Langmuir et al., 1992; McKenzie and Bickle, 1988). As discussed above, the effect of clinopyroxene and plagioclase on whole-rock major element compositions of the Changpu basalts with MgO >6.0 wt.% and Fankeng basalts with MgO >7.0 wt.% can be ignored and olivine was the dominant phase within the assemblage of crystallizing minerals (Fig. 7a–d). Crustal contamination was also insignificant (Fig. 7e,f). To minimize the potential minor effect of crystallisation and contamination, only samples with MgO ≥7.0 wt.% were chosen as starting materials to reconstruct the primary melt composition for the Changpu and Fankeng basalts. Samples with MgO <8 wt.% were given the $Fe_{8.0}$ and $Na_{8.0}$ expressions of Klein and Langmuir (1987) to correct the MgO, FeO and Na_2O concentrations. Kelley et al. (2006) showed that most melts with MgO <8.5 wt.% are still on the olivine + plagioclase cotectic and adding olivine at this point would lead to a false high FeO content. To further remove the effect of plagioclase, expressions of Kelley et al. (2006) were employed to make an additional fractionation correction to 8.5 wt.% MgO. Samples with MgO between 8.0 and 8.5 wt.% were corrected to 8.5 wt.% MgO only along this linear olivine + plagioclase cotectic (Kelley et al., 2006). These 8.5 wt.% MgO-equivalent compositions and samples with initial MgO >8.5 wt.% were chosen as starting compositions.

A series of olivine and basalt compositions were then calculated from these starting materials applying the method proposed by X.C. Wang et al. (2012), as follows: (1) the composition of equilibrium olivine was obtained using $K_D(Fe/Mg)^{ol/liq} = 0.3$ (Roeder and Emslie, 1970), assuming Fe^{2+}/total Fe = 0.9; (2) a more primitive basalt composition

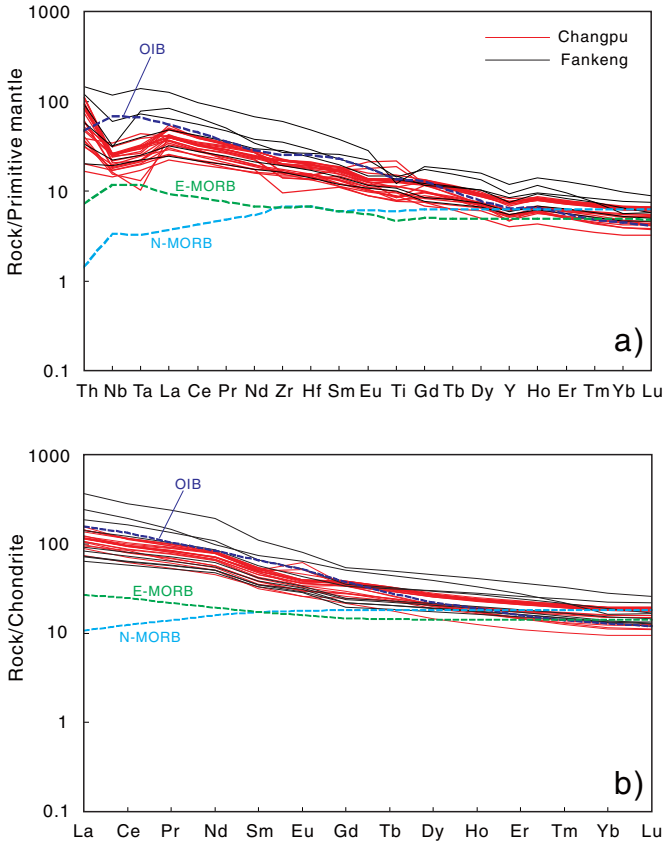

Fig. 6. (a) Primitive mantle normalized multiple trace elements and (b) chondrite-normalized REE distribution patterns of the Changpu and Fankeng basalts. Normalization values and OIB, MORB data are from Sun and McDonough (1989).

was calculated as a mixture of the basalt and equilibrium olivine at a weight ratio of 99:1; (3) steps (1) and (2) were repeated until the equilibrium olivine was in equilibrium with Fo89. All calculated samples required <25% olivine addition to reach Fo89 equilibrium.

The modeled primary melt compositions are presented in Table 3. The calculated primary melts have MgO varying from 15.0 to 16.0 wt.%, SiO_2 ranging from 48.6 to 49.0 wt.% and FeO^T from 11.1 to 11.6 wt.%. Effective melting pressure (P_f) is estimated at 1.9–2.1 GPa by applying the method of Lee et al. (2009), suggesting that the magmas were generated at depths of 60–70 km. Applying the methods of Beattie (1993), the erupting temperatures were estimated at 1348 °C to 1369 °C with an average of 1356 °C. The melting temperature is calculated as 1453 °C–1480 °C (average 1456 °C) using the approach of Lee et al. (2009). The mantle potential temperature, T_P (Mckenzie and Bickle, 1988), is estimated at 1458 °C–1482 °C (average 1475 °C) using the equation T_P (°C) = 1463 + 12.74*MgO wt.% − 2924/MgO wt.% (Herzberg and O'Hara, 2002).

It is noteworthy that neither of the two estimation models takes into account the effect of water, which is another factor that influences the melting temperature and pressure. H_2O concentration in melts can be estimated using their primary Ce, assuming that the basalts have the same H_2O/Ce ratio of ~200 as oceanic basalts (Herzberg et al., 2007). The calculated H_2O concentrations are constant at 0.69 wt.% based on the Ce contents of all five basalt samples. If we accept the highest value of H_2O/Ce (~300) from oceanic basalts (Dixon et al., 2002; Michael, 1995), the calculated H_2O concentration is 1.04 wt.%. The effect of H_2O on the olivine liquidus temperature was demonstrated as the liquidus depression temperature (°C) = $74.403^*(H_2O\ wt.\%)^{0.352}$ (Falloon and Danyushevsky, 2000). Approximately 1.04 wt.% H_2O would suppress the melt temperature by ~75 °C relative to the anhydrous system. Therefore, the estimated mantle potential temperature for the melting region is 1383 °C–1407 °C (1400 °C on average), similar to modern MORB ambient mantle ~1350 ± 50 °C (e.g., Herzberg et al., 2007; Lee et al., 2009).

In summary, the estimated melting conditions and mantle potential temperature imply asthenospheric upwelling and large-scale lithosphere extension.

5.4. Origin of the Early Jurassic basalts

As discussed above, the presence of an OIB-type high-Nb/La end-member melt and asthenospheric mantle-derived chemical signatures suggests that the asthenospheric mantle was the dominant reservoir for the Early Jurassic Changpu and Fankeng basalts. This is consistent with evidence from the contemporaneous Chenglong (182 Ma; He et al., 2010), Chebu (173 Ma; Li et al., 2003) and Xialan (193–195 Ma; Zhu et al., 2010) gabbros that were mainly derived from the asthenosphere mantle (Zhu et al., 2010; He et al., 2010).

The degree of fractionation of REEs is usually used to constrain melting depth (spinel- versus garnet-peridotite). Heavy rare earth elements (HREEs) are more compatible in garnet than in spinel, but light REEs have similar compatibilities in these two minerals (Mckenzie and O'Nions, 1991). Therefore, the ratios of LREE/HREE (La/Yb) and middle REE/HREE (Dy/Yb) can provide an important constraint on melting depth (X.W. Li et al., 2013; Jiang et al., 2005; Tschegg et al., 2011). Neither crustal contamination nor low-pressure fractional crystallization can effectively modify these ratios, but partial melting or source mixing can affect these ratios (Tschegg et al., 2011; Jung et al., 2012; X.W. Li et al., 2013). Primary Yb contents were obtained with a Rayleigh crystal fractionation model by using the fraction of liquid (F) obtained from the olivine addition modelling (X.C. Wang et al., 2012). As shown in Fig. 9 (a, b, c), the trend of the samples can be duplicated by mixing between spinel- and garnet-bearing peridotite-derived melt, indicating melting at the depth of the spinel–garnet transition. Our modelling shows that the primary magma can be produced by mixing 15% partial melting of spinel lherzolite with 2% partial melting of garnet lherzolite (Fig. 9b,c). Moreover, the Sm/Yb–Ce/Yb correlation indicates that the primary melts were mainly produced at about 50–70 km (Fig. 9d). This is similar to the Emeishan low-Ti basalts, which were interpreted to have formed at the spinel–garnet transition zone (Xu et al., 2001). Such a constraint from fractionation of REEs agrees well with the estimated melting depth by primary major element compositions (about 60–70 km, 1.9–2.1 GPa) using the method of Lee et al. (2009).

Table 2
Results of Sr–Nd isotopic compositions for the Changpu basalts in southern Jiangxi Province.

Samples	Rb (ppm)	Sr (ppm)	$^{87}Rb/^{86}Sr$	$^{87}Sr/^{86}Sr$	$\pm 2\sigma$	$(^{87}Sr/^{86}Sr)_i$	Sm (ppm)	Nd (ppm)	$^{147}Sm/^{144}Nd$	$^{143}Nd/^{144}Nd$	$\pm 2\sigma$	$\varepsilon Nd(t)$
08GN05-2	24.9	218	0.33	0.711069	0.000010	0.71017	5.04	21.2	0.144	0.512441	0.000006	−2.56
08GN05-4	16.2	294	0.16	0.710654	0.000010	0.71022	5.41	25.2	0.130	0.512309	0.000006	−4.79
08GN14-2	18.6	172	0.80	0.710650	0.000010	0.70848	8.05	37.8	0.129	0.512416	0.000006	−2.71
08GN14-3	99.1	358	0.31	0.710275	0.000010	0.70943	8.26	38.6	0.129	0.512409	0.000006	−2.82
08GN32-7	26.8	279	0.28	0.709822	0.000012	0.70907	4.84	23.5	0.125	0.512382	0.000008	−3.25
08GN32-8	127	327	1.12	0.711483	0.000008	0.70846	6.49	30.7	0.128	0.512476	0.000008	−1.48
08GN34-1	16.2	296	0.16	0.709004	0.000010	0.70858	7.45	33.0	0.136	0.512513	0.000006	−0.98
08GN45-1	20.1	481	0.12	0.708621	0.000010	0.70829	6.91	31.4	0.133	0.512471	0.000006	−1.71

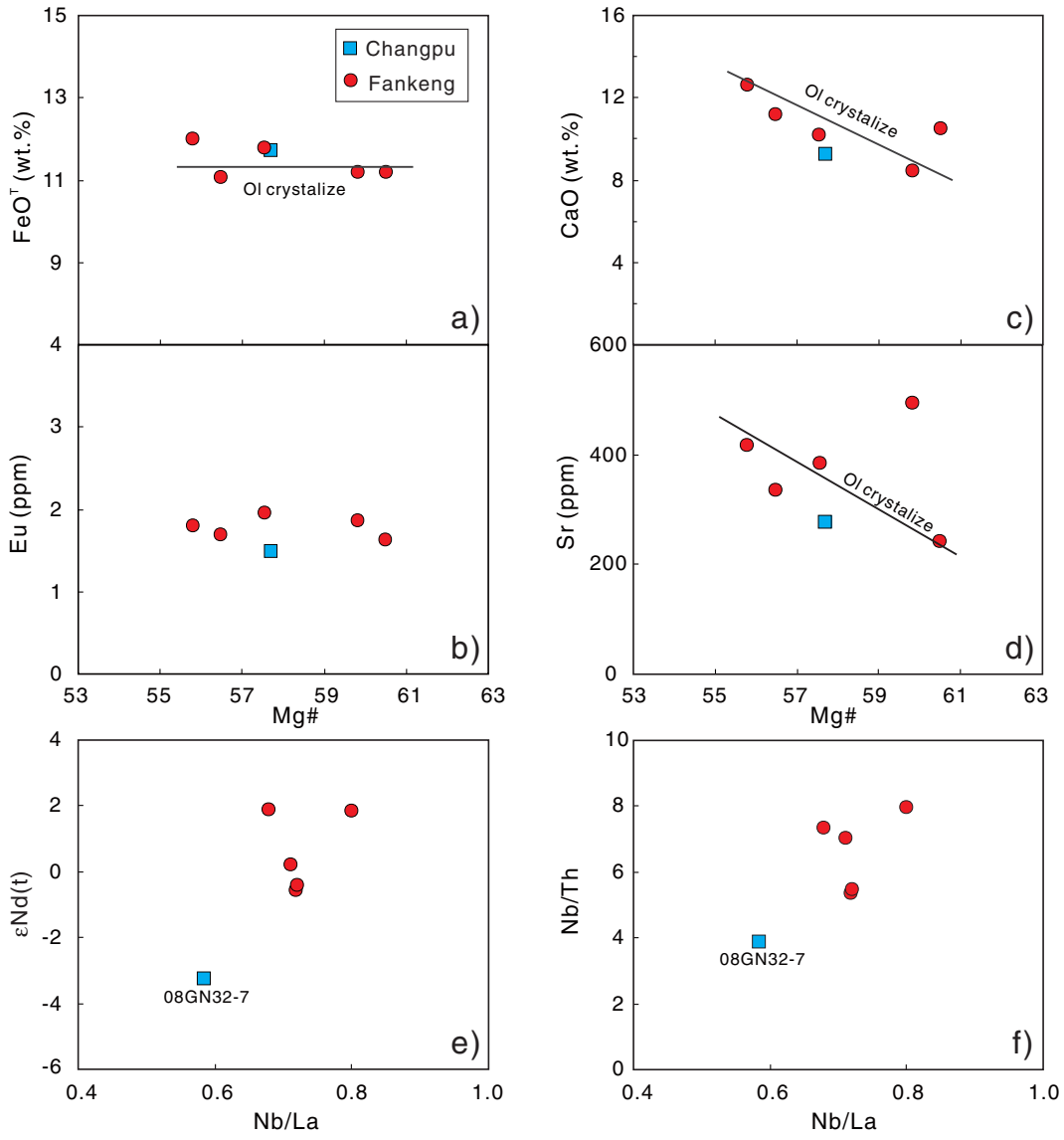

Fig. 7. (a–d) Variation of Mg$^{\#}$ with FeO^T, CaO, Eu and Sr contents. (e–f) Variation of Nb/La with εNd(t) and Nb/Th.

Although the mantle source lithology of basaltic magma has long been assumed to be dominated by peridotite (e.g., Green and Ringwood, 1963; O'Hara, 1967), recent studies have shown that pyroxenites/eclogites play an important role in the source of oceanic island basalts and continental flood basalts (e.g., Sobolev et al., 2005, 2007; Herzberg, 2011; X.C. Wang et al., 2012, 2014; Heinonen et al., 2013). Zn/Fe and Fe/Mn ratios are promising proxies for discriminating a pyroxenite from a peridotite source (Le Roux et al., 2010; Ferguson et al., 2013; Zhang et al., 2015). Most of our samples have Zn/Fe and Fe/Mn ratios similar to peridotite melts (Fig. 10a,b), indicating a dominant peridotitic source for the basalts. Furthermore, by comparing with experimental melts (Fig. 10c,d), the estimated primary melts could be produced by partial melting of volatile-free peridotite.

Together, these observations provide important constraints on the thickness of the continental lithosphere. Because these basalts were mainly derived from the asthenospheric mantle at <70 km depth, the thickness of the lithosphere must have been thinned to less than 70 km before 190 Ma. This suggests that at least 30 km of the base of the lithosphere was removed before this time. Therefore, asthenospheric upwelling and/or delamination may have attributed to large-scale lithospheric extension.

5.5. Geological implications

5.5.1. Timing and duration of Early Jurassic magmatism

The spatial and temporal distribution of magmatic events is crucial for understanding geological and geodynamic processes. Much geochronological work has been done on the Early Jurassic volcanic/intrusive rocks in southern Jiangxi Province and adjacent regions. Previous Rb–Sr and K–Ar ages of the volcanic rocks suggested that the volcanic suites were erupted predominantly between 180 and 160 Ma (Chen et al., 1999a, 1999b; Y.J. Wang et al., 2003). However, recent zircon U–Pb geochronology of the volcanic rocks of the Changpu–Baimianshi and the Dongkeng–Linjiang basins yielded older ages of 195–191 Ma (Ji and Wu, 2010; Xiang and Wu, 2012). Our new zircon U–Pb ages from the Changpu–Baimianshi and the Dongkeng–Linjiang volcanic sections are consistent with these published zircon U–Pb ages. Our age samples were collected from the bottom to the top of this volcanic rock succession; therefore, our zircon U–Pb ages suggest that basin-scale eruptions occurred during a time interval of ≤5 Ma (Fig. 11a), probably even ≤2 Ma. Regionally, Early Jurassic volcanic and intrusive rocks formed predominantly between 195 and 185 Ma. The significantly younger Rb–Sr and K–Ar ages were likely due to overprinting by the younger magmatic-thermal events (Fig. 11a, b).

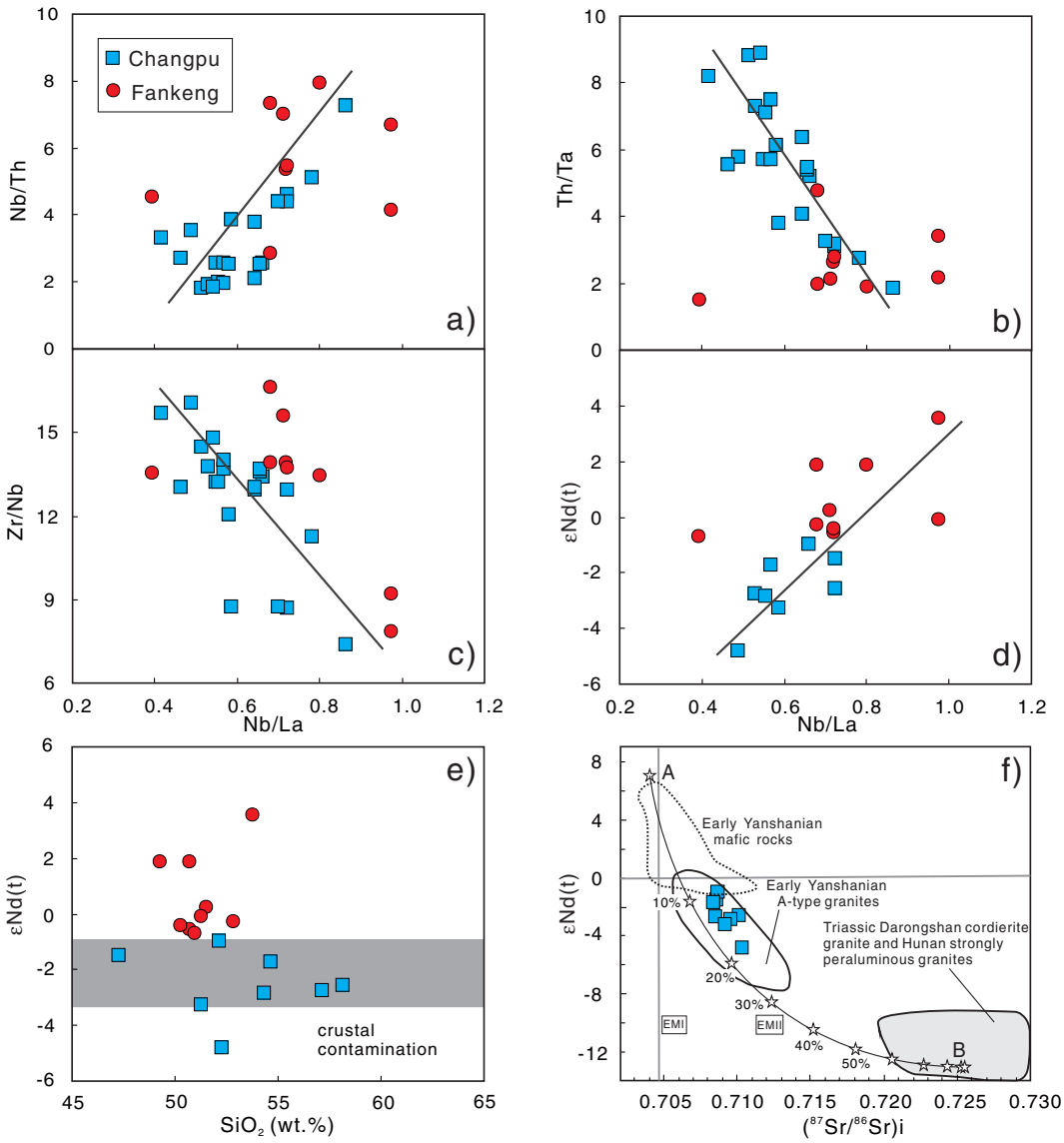

Fig. 8. (a–d) Variation of Nb/La with Nb/Th, Th/Ta, Zr/Nb and εNd(t). (e) Variation of SiO_2 with εNd(t), and (f) AFC modelling for Sr–Nd isotope evolution. A represents a depleted mantle member with Sr = 375 ppm, Nd = 24.8 ppm, εNd(t) = 7, I_{Sr} = 0.704 (after Zhu et al., 2010); B represents a crustal member with Sr = 109 ppm, Nd = 39.6 ppm, εNd(t) = −13.1, I_{Sr} = 0.7255 (Darongshan granite 22GX12 ; Hsieh et al., 2008). The partition coefficient for Sr and Nd between minerals and melt used for the fractional crystallization are: D^{Sr} = 0.7027 and D^{Nd} = 0.6382, and corresponding mineral assemblage is Cpx/Pl/Mt/Ol = 40/38/16/6 (Zhu et al., 2010). Sr–Nd isotope compositions of the Triassic Darongshan cordierite granite and the Hunan strongly peraluminous granite (Wang et al., 2007a; Hsieh et al., 2008) are also shown. The AFC trend (pentagram marks) are shown at 0.1 intervals.

Table 3
Calculated major elements and thermal parameters for selected samples after stripping off effect of potential water content.

Sample	08GN32-7	PK-4	PK-7	PK-9	TB-2
SiO_2	48.78	48.90	48.64	48.58	48.98
TiO_2	1.38	1.72	1.59	1.81	1.56
Al_2O_3	11.30	11.71	11.18	11.22	11.44
FeO^T	11.59	11.06	11.64	11.64	11.24
MnO	0.16	0.16	0.17	0.16	0.17
MgO	15.97	15.05	16.02	15.94	15.40
CaO	8.34	8.15	8.47	8.43	8.83
Na_2O	1.64	2.84	1.43	1.81	1.51
K_2O	0.66	0.63	0.69	0.64	0.68
P_2O_5	0.18	0.18	0.17	0.18	0.18
Added Ol (%)	22	19	22	22	20
T_P (°C)	1406	1383	1407	1406	1391
T_1 (°C)	1292	1273	1294	1292	1280
T_2 (°C)	1402	1378	1405	1405	1385
P (Ga)	2.04	2.12	2.04	2.14	1.86

T_P represents mantle potential temperature; T_1 represents erupting temperature; T_2 represents melting temperature; P represents the effective melting pressure. The water effect was considered during all temperature calculations.

5.5.2. Basin and Range-type lithospheric and mantle thermal state?

Primary compositions of basalts reflect temperatures and pressures of magma generation, providing windows into the thermal state of the mantle (Mckenzie and Bickle, 1988; Lee et al., 2009). Basalts can be formed at constructive plate margins (MOR basalts), destructive plate margins (arc magma) and within plates (OIB, CFB and CRM), each showing distinctive mantle thermal characteristics (Lee et al., 2009).

As discussed above, the calculated mantle potential temperature for the Early Jurassic basalts from the study area is within the range of 1383 °C–1407 °C (average 1400 °C) and pressure 1.9–2.1 GPa (60–70 km), marginally higher than that of average MOR basalts, suggesting a slightly hotter mantle in this region. The estimated average temperature of 1400 °C is lower than the expected temperature of >1500 °C for a typical hotspot (Lee et al., 2009), suggesting a non-plume origin. The cause of the elevated temperature was probably deep asthenospheric mantle upwelling. The tholeiitic character of the Early Jurassic basalts is therefore attributed to a slightly hotter mantle temperature at a shallower depth. Moreover, because the 190 Ma

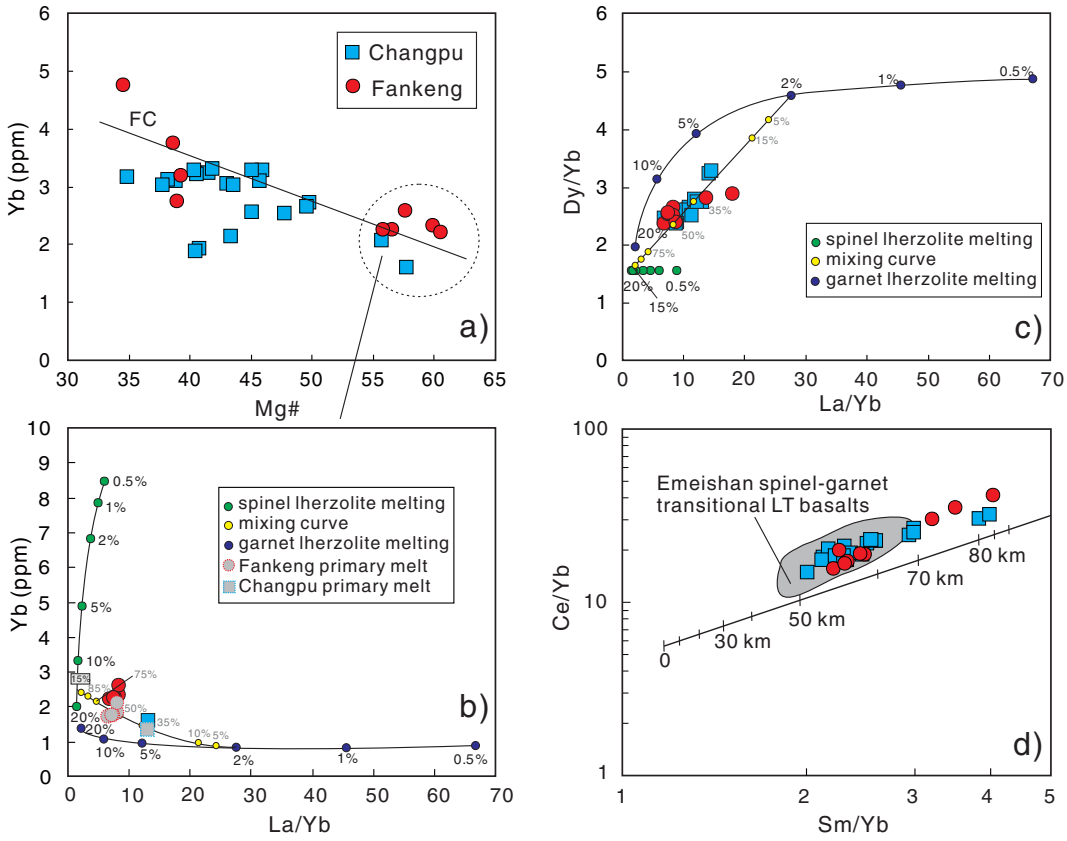

Fig. 9. (a) $Mg^{\#}$ versus Yb, (b–c) Qualitative and semi-qualitative partial melting models based on La/Yb versus Yb and Dy/Yb, and (d) Sm/Yb versus Ce/Yb. The partial melting modeling in (b,c) and (d) was conducted according to Tschegg et al. (2011) and Ellam (1992), respectively. Data source of Emeishan basalts is from Xu et al. (2001).

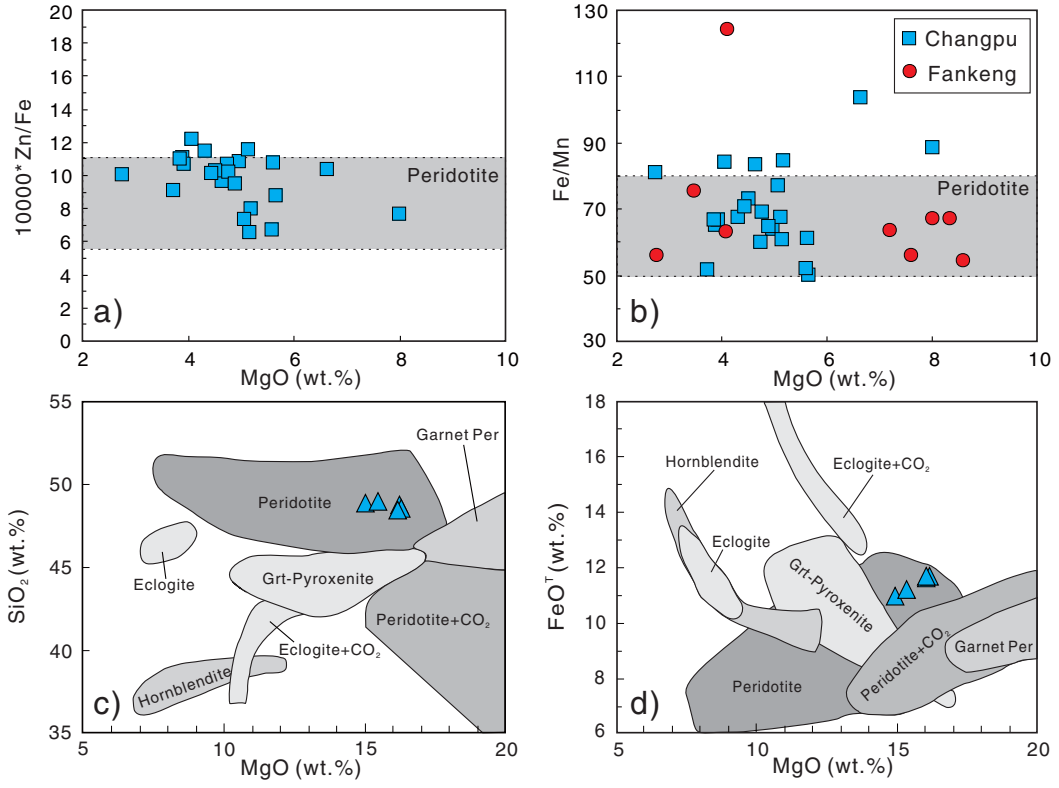

Fig. 10. (a,b) MgO versus Zn/Fe and Fe/Mg diagrams, Zn/Fe and Fe/Mn ratios of mantle peridotite-derived melts are according to Ferguson et al. (2013) and Le Roux et al. (2010). (c,d) MgO versus SiO_2 and FeO^T diagrams, the high-pressure experimental melts determined melts performed by various starting materials are also shown (modified after Xu et al., 2012). Triangles represent calculated primary magmas of the Early Jurassic basalts, southern Jiangxi Province. Data sources: volatile-free peridotite from Hirose and Kushiro (1993); CO_2-bearing peridotite from Dasgupta et al. (2007); carbonated eclogite from Dasgupta et al. (2006); garnet pyroxenite from Hirschmann et al. (2003); hornblendite from Pilet et al. (2008).

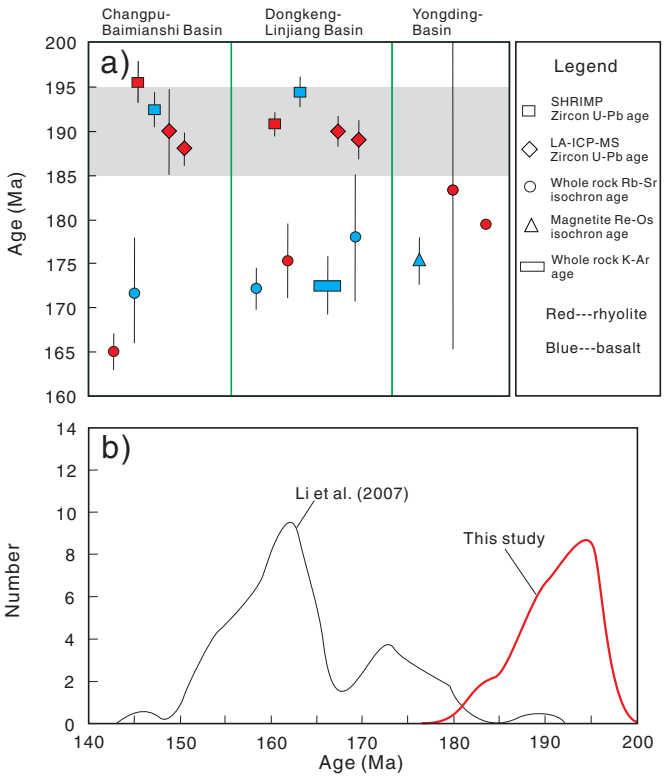

Fig. 11. (a) Ages of the Changpu and Fankeng bimodal volcanics were determined by different methods. (b) Statistic comparison of zircon U–Pb ages from the Early Jurassic volcanic rocks, southern Jiangxi Province with previously compiled ages of Jurassic volcanics and intrusive rocks in South China (modified after X.H. Li et al., 2012). Ages are from Chen et al. (1999b, 2004), Y.J. Wang et al. (2003); Zhou et al. (2005a, 2005b)), Li and Li (2007); Ji and Wu (2010); Yu et al. (2010); Xiang and Wu (2012); Zhu et al. (2010) and He et al. (2010).

basalts were derived mainly from depleted asthenospheric mantle with an effective melting pressure of 1.9–2.1 GPa, the thickness of the lithosphere in this region was less than 70 km. Our estimated mantle potential temperatures are comparable with those of the present-day western Basin and Range Province (Fig. 12), which has potential

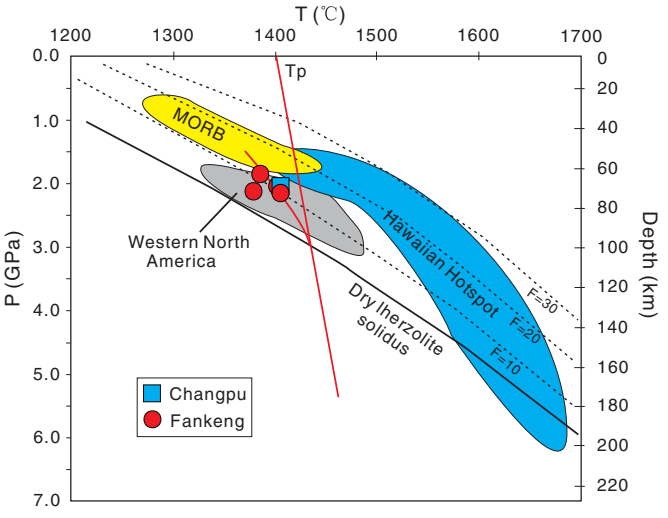

Fig. 12. Temperatures and pressures calculated for the Changpu and Fankeng basalts. Lherzolite solidus and melt fraction isopleths are from Katz et al. (2003). Curved lines represent melting adiabats. Near-vertical line represents solid mantle adiabats. Fields for MORB, Hawaiian Hotspot and Western North America are from Lee et al. (2009).

temperatures of 1350 °C–1450 °C and pressures of 2–3 GPa (60–90 km) (Wang et al., 2002).

5.5.3. Post-orogenic extensional tectonic environment

The petrogenesis of Early Jurassic magmatic rocks in South China is important for understanding the Mesozoic tectonic evolution of the region, but the topic is, at present, highly controversial. Xie et al. (2001) used a mantle plume model to explain the Early Jurassic rifting/extension. However, our estimated mantle potential temperature argues against such a model. Furthermore, a mantle plume should have produced a large volume of flood basalts and continental-scale doming, neither of which has been observed in the Mesozoic of South China. Although a rifting and lithospheric extension model was widely accepted for explaining the petrogenesis of the within-plate magmatism (Chen et al., 1999a, 1999b; Li et al., 2003, 2004; Li and Li, 2007; Y.J. Wang et al., 2005, 2013; Yu et al., 2010), this does not provide a feasible geodynamic mechanism for the event.

The presence of an active continental margin along the southeastern margin of the South China Block during much of the Mesozoic has been widely accepted (e.g., Cui and Li, 1983; Jahn et al., 1990; Zhou and Li, 2000; Carter et al., 2001). The initial arc magmatism started at ca. 280 Ma, as evidenced by the 267–262 Ma Wuzhishan granites in Hainan Island at the southern margin of the South China Block (Li et al., 2006) and the ca. 280 Ma detrital zircon age peak from both the South China hinterland (X.H. Li et al., 2012) and Taiwan (Z.X. Li et al., 2012). Li and Li (2007) and Z.X. Li et al. (2012) proposed a flat-slab subduction model for South China during the Mesozoic. This model explains the hinterland orogeny in South China during the Late Permian to Early Jurassic in a similar manner to the Laramide Orogen in western North America (Coney and Reynolds, 1977; Dickinson and Snyder, 1978; Bird, 1998). The collapse of the broad orogen was used to explain the formation of a Basin and Range-style magmatic province in South China during the Jurassic–Cretaceous (Li and Li, 2007).

In the Mesozoic of South China, mountain building occurred mainly during the Middle Triassic. By the Late Triassic, orogenic activity occurred mainly in the continental interior some 1300 km from the active plate margin. In addition, a broad intracontinental basin, evolved from a terrestrial sag basin to a shallow-marine basin during the Late Triassic–Early Jurassic over the Middle Triassic orogen (Li and Li, 2007; Pang et al., 2014). Early Jurassic shallow-marine deposition corresponds to the emplacement of the bimodal volcanic rocks in the Changpu–Baimianshi basin in southern Jiangxi Province (Li and Li, 2007; Pang et al., 2014). Our estimated mantle potential temperature and pressure for the volcanic rocks suggests a relatively thin lithosphere and asthenospheric upwelling in the centre of South China during the Early Jurassic (~190 Ma). The associated Early Jurassic basaltic magmatism formed by asthenospheric upwelling under thinned continental lithosphere and may therefore signify the first petrologic response to breakup and foundering of the flat oceanic slab after basalt to eclogite transformation, as suggested by Li and Li (2007). Indeed, this event coincided with the termination of shallow marine deposition in that region and the beginning of graben formation (Pang et al., 2014).

6. Conclusions

We draw the following conclusions based on our new results:

1) LA–ICP–MS zircon U–Pb dating indicates that the Jurassic rhyolite in southern Jiangxi Province erupted at 188–195 Ma. They have bimodal association with tholeiitic basalts and are characterized by a short time interval (≤5 Ma) eruption lifetime across several local basins, and were part of a ca. 10 Ma (195–185 Ma) regional-scale magmatic event.
2) The geochemical characteristics of the basalts indicate that they were derived from asthenospheric mantle, and the melts experienced fractionated crystallization and variable degrees of SCLM contamination.

3) Numerical simulation results constrain a partial melting pressure of 1.9–2.1 GPa and an average mantle potential temperature at 1400 °C, slightly hotter than the normal MORB–source mantle but resembling that of the Basin and Range Province in western USA.
4) The existence of a Basin and Range-type lithosphere of South China during the Early Jurassic likely signifies the lithospheric response to flat-slab breakup and foundering.

Acknowledgements

We would like to thank Simon Wilde (Curtin University) for his constructive suggestions, fruitful discussions and careful proofreading; Camilla Stark (Curtin University) for proofreading an early version; Y. Liu, X.L. Tu, and Z.Y. Ren for their assistance in geochemical and Sr–Nd isotopic analyses, and H. Zhang for LA–ICP–MS U–Pb zircon analyses. Comments and suggestions from two anonymous reviewers and editor in-chief Andrew Kerr greatly improved the paper. This work was supported by the NSFC (grants 40973025, 41173039 and 41373033) and the Chinese Geological Survey (grants 1212011085446 and 12120113070800) and the Australian Research Council (ARC) grants (DP110104799 and FL150100133) to Z.X. Li and ARC Future Fellowship (FT140100826) to X.C. Wang. This is GIGCAS contribution NO. IS-2220 and contribution 804 of ARC Centre of Excellence for Core to Crust Fluid Systems.

Appendix A

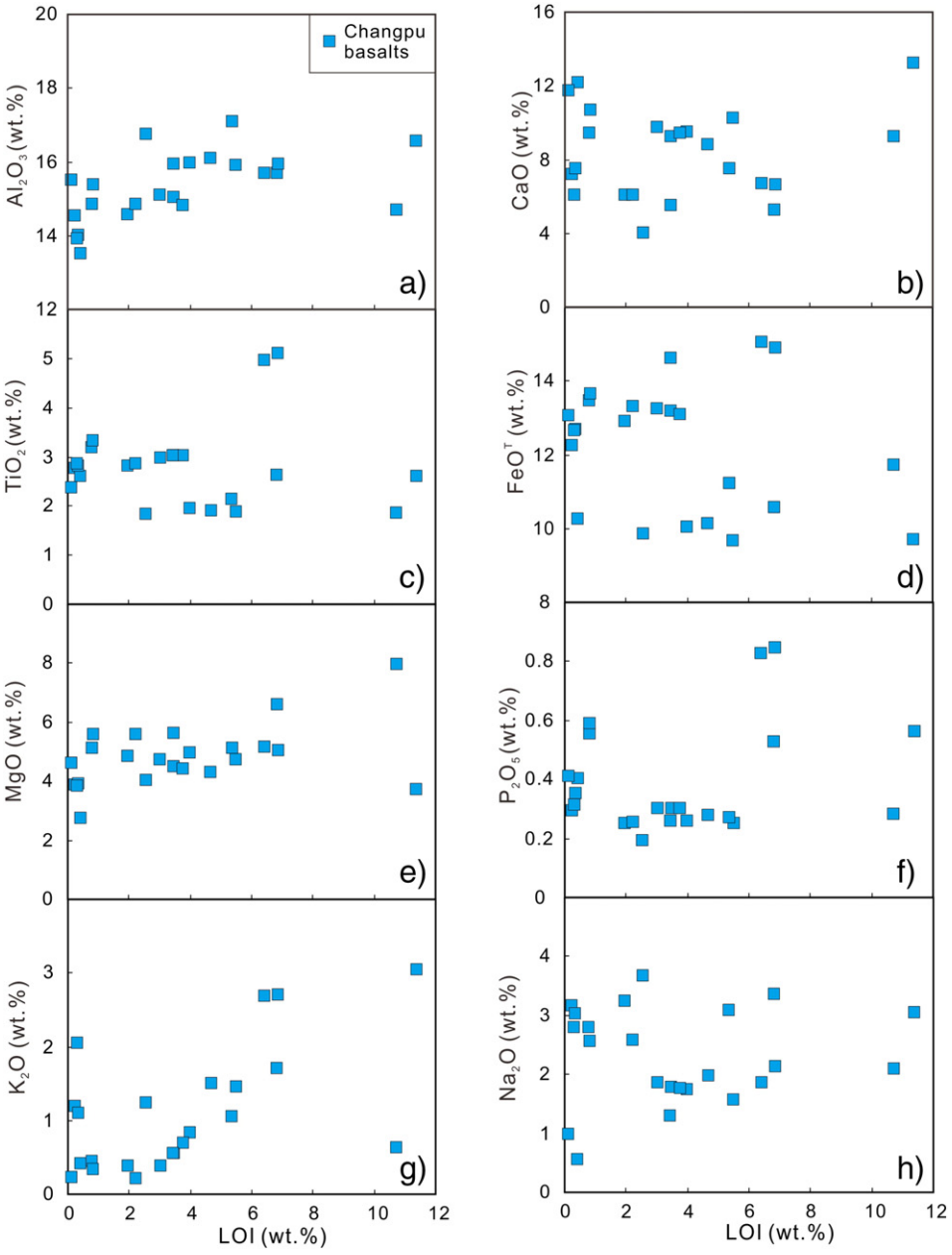

Appendix Fig. A-1. Major elements versus LOI variation diagrams showing the effects of alteration on major elements.

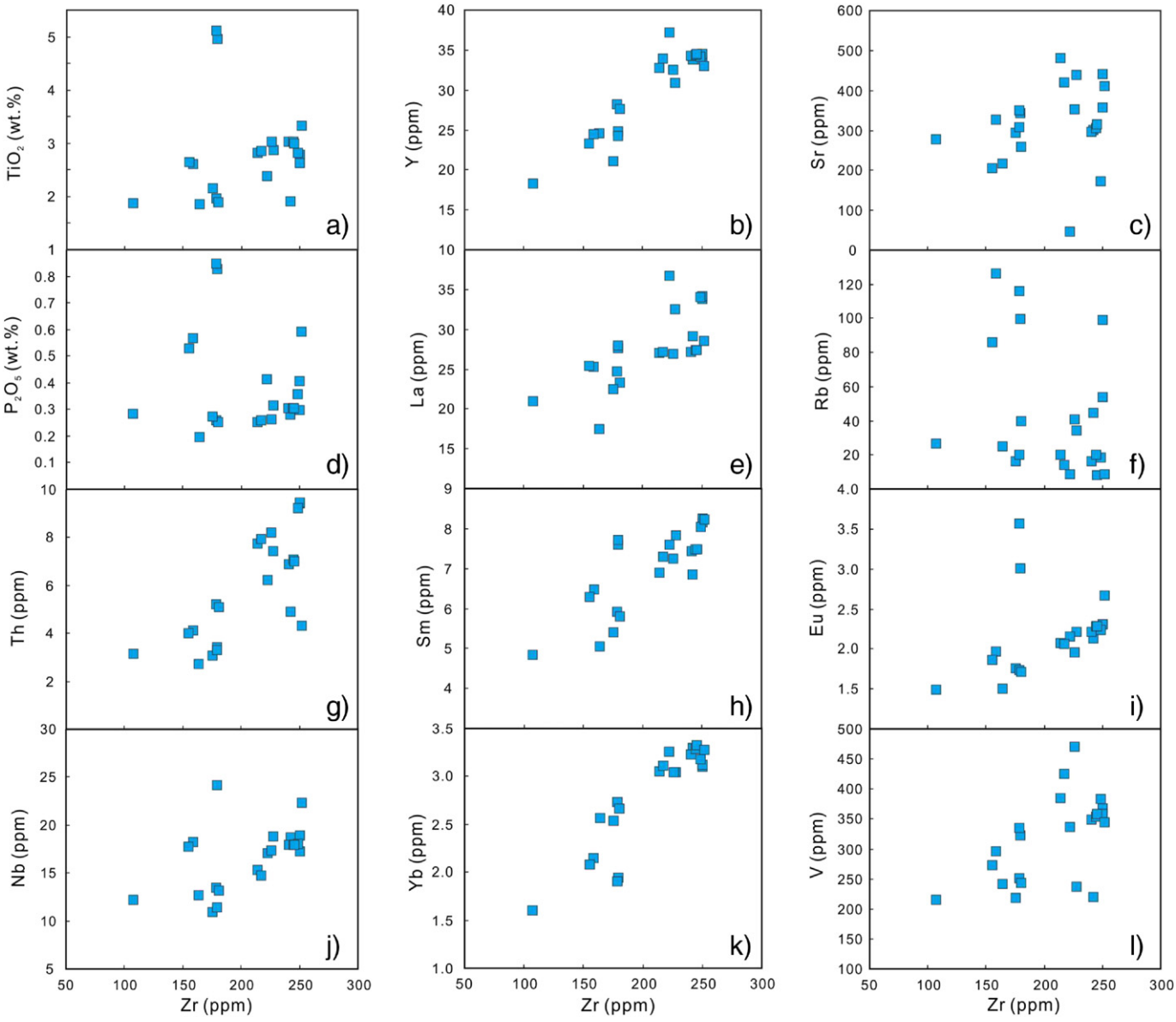

Appendix Fig. A-2. Selected major and trace elements versus Zr variation diagrams showing the effects of alteration on major and trace elements.

Appendix Table 1
LA–ICP–MS zircon U–Pb isotopic analyses for rhyolites from the Changpu–Baimianshi and Dongkeng–Linjiang basins.

Analysis	Th	U		Isotopic ratio						Age (Ma)			
	(ppm)	(ppm)	Th/U	$^{207}Pb/^{206}Pb$	± 1σ	$^{207}Pb/^{235}U$	± 1σ	$^{206}Pb/^{238}U$	± 1σ	$^{207}Pb/^{235}U$	± 1σ	$^{206}Pb/^{238}U$	± 1σ
08GN04-1													
08GN04-1-01	107	47	2.26	0.0580	0.0152	0.2481	0.0570	0.02887	0.00161	225	46	183	10
08GN04-1-02	76	38	1.98	0.1405	0.0378	0.5075	0.1167	0.02996	0.00166	417	79	190	10
08GN04-1-03	76	42	1.78	0.0869	0.0208	0.3367	0.0907	0.03033	0.00147	295	69	193	9
08GN04-1-04	329	133	2.47	0.0891	0.0104	0.3725	0.0445	0.03002	0.00107	322	33	191	7
08GN04-1-05*	94	43	2.18	0.1338	0.0206	0.6148	0.0911	0.03535	0.00178	487	57	224	11
08GN04-1-06	130	57	2.27	0.1852	0.0911	0.3751	0.0839	0.03045	0.00188	323	62	193	12
08GN04-1-07*	415	520	0.80	0.0533	0.0027	0.4967	0.0247	0.06765	0.00129	409	17	422	8
08GN04-1-08**	138	57	2.41	0.1003	0.0191	0.3568	0.0706	0.02732	0.00129	310	53	174	8
08GN04-1-09**	136	62	2.21	0.0848	0.0209	0.2910	0.0785	0.02676	0.00132	259	62	170	8
08GN04-1-10	60	36	1.65	0.0679	0.0192	0.2517	0.0621	0.03013	0.00182	228	50	191	11
08GN04-1-11*	54	30	1.79	0.1181	0.0403	0.3795	0.1086	0.03282	0.00189	327	80	208	12
08GN04-1-12	220	87	2.53	0.0911	0.0239	0.3084	0.0672	0.02968	0.00125	273	52	189	8
08GN04-1-13	68	36	1.91	0.1556	0.0279	0.5995	0.1016	0.03016	0.00146	477	65	192	9
08GN04-1-14	103	47	2.22	0.1174	0.0410	0.4224	0.1160	0.02995	0.00137	358	83	190	9
08GN04-1-15	84	44	1.92	0.1364	0.0359	0.4781	0.1219	0.03003	0.00176	397	84	191	11
08GN04-1-16*	67	37	1.81	0.2529	0.0427	2.4309	0.5522	0.04635	0.00479	1252	165	292	29
08GN04-1-17	68	36	1.91	0.1825	0.0327	0.7238	0.1367	0.03003	0.00177	553	81	191	11
08GN04-1-18	115	49	2.34	0.0719	0.0186	0.3337	0.0846	0.02999	0.00152	292	65	191	10

Appendix Table 1 (*continued*)

Analysis	Th	U		Isotopic ratio						Age (Ma)			
	(ppm)	(ppm)	Th/U	$^{207}Pb/^{206}Pb$	± 1σ	$^{207}Pb/^{235}U$	± 1σ	$^{206}Pb/^{238}U$	± 1σ	$^{207}Pb/^{235}U$	± 1σ	$^{206}Pb/^{238}U$	± 1σ
08GN07-1													
08GN07-1-01	477	415	1.15	0.0636	0.0058	0.2727	0.0294	0.02987	0.00072	245	23	190	4
08GN07-1-02	71	98	0.72	0.0562	0.0110	0.2187	0.0361	0.02960	0.00097	201	30	188	6
08GN07-1-03*	305	936	0.33	0.0475	0.0023	0.2359	0.0120	0.03571	0.00068	215	10	226	4
08GN07-1-04	98	120	0.81	0.0960	0.0117	0.3925	0.0474	0.02976	0.00089	336	35	189	6
08GN07-1-05	67	96	0.69	0.0439	0.0095	0.1783	0.0396	0.02973	0.00102	167	34	189	6
08GN07-1-06	58	86	0.67	0.0805	0.0121	0.3073	0.0459	0.02882	0.00097	272	36	183	6
08GN07-1-07	121	129	0.94	0.0622	0.0100	0.2416	0.0367	0.02864	0.00087	220	30	182	5
08GN07-1-08	425	381	1.12	0.0474	0.0038	0.1945	0.0156	0.02941	0.00062	180	13	187	4
08GN07-1-09	277	332	0.83	0.0505	0.0053	0.2093	0.0219	0.02994	0.00063	193	18	190	4
08GN07-1-10	117	126	0.93	0.0676	0.0109	0.2599	0.0401	0.02884	0.00094	235	32	183	6
08GN07-1-11*	260	441	0.59	0.0767	0.0050	1.6732	0.1053	0.15464	0.00269	998	40	927	15
08GN07-1-12	109	128	0.85	0.0647	0.0089	0.2725	0.0365	0.02999	0.00097	245	29	191	6
08GN07-1-13	80	102	0.79	0.0586	0.0114	0.2254	0.0379	0.02952	0.00113	206	31	188	7
08GN07-1-14	117	124	0.94	0.0882	0.0104	0.3684	0.0437	0.02988	0.00092	318	32	190	6
08GN07-1-15	253	270	0.94	0.0638	0.0060	0.2515	0.0235	0.02815	0.00062	228	19	179	4
08GN07-1-16	78	103	0.76	0.0639	0.0111	0.2547	0.0416	0.02922	0.00085	230	34	186	5
08GN07-1-17	77	97	0.79	0.0618	0.0114	0.2463	0.0471	0.02788	0.00089	224	38	177	6
08GN07-1-18	81	101	0.81	0.0572	0.0116	0.2329	0.0458	0.02975	0.00105	213	38	189	7
08GN07-1-19	340	513	0.66	0.0520	0.0044	0.2291	0.0184	0.03151	0.00067	209	15	200	4
08GN07-1-20	89	111	0.80	0.0587	0.0101	0.2511	0.0446	0.02998	0.00118	227	36	190	7
08GN07-1-21	70	99	0.71	0.0629	0.0137	0.2403	0.0502	0.02898	0.00110	219	41	184	7
08GN07-1-22	64	90	0.71	0.0548	0.0089	0.2277	0.0378	0.03030	0.00093	208	31	192	6
08GN07-1-23	341	288	1.18	0.0470	0.0050	0.1981	0.0200	0.03052	0.00073	184	17	194	5
08GN07-1-24	79	101	0.78	0.0892	0.0112	0.3504	0.0425	0.02972	0.00107	305	32	189	7
08GN07-1-25**	192	188	1.02	0.1560	0.0989	0.5702	0.3585	0.02727	0.00073	458	236	173	5
08GN32-1													
08GN32.1-1	48	81	0.60	0.0772	0.0139	0.2916	0.0495	0.03033	0.00115	260	39	193	7
08GN32.1-2	114	269	0.42	0.0470	0.0054	0.1910	0.0207	0.03001	0.00067	177	18	191	4
08GN32.1-3	146	202	0.72	0.0695	0.0073	0.2982	0.0347	0.03009	0.00077	265	27	191	5
08GN32.1-4	313	262	1.19	0.0809	0.0104	0.3197	0.0403	0.02895	0.00073	282	31	184	5
08GN32.1-5	152	366	0.41	0.0869	0.0099	0.3760	0.0482	0.03019	0.00084	324	36	192	5
08GN32.1-6	113	228	0.49	0.0528	0.0060	0.2066	0.0221	0.02962	0.00083	191	19	188	5
08GN32.1-7	202	573	0.35	0.0472	0.0034	0.1949	0.0131	0.02994	0.00062	181	11	190	4
08GN32.1-8	172	437	0.39	0.0544	0.0046	0.223	0.0189	0.02959	0.00065	204	16	188	4
08GN32.1-9	146	323	0.45	0.0731	0.0091	0.3018	0.0371	0.02993	0.00062	268	29	190	4
08GN32.1-10	92	115	0.80	0.0955	0.0142	0.3994	0.0648	0.02966	0.00109	341	47	188	7
08GN32.1-11	123	298	0.41	0.0377	0.0054	0.1544	0.0235	0.03000	0.00084	146	21	191	5
08GN32.1-12	136	374	0.36	0.0442	0.0047	0.1843	0.0199	0.03013	0.00066	172	17	191	4
08GN32.1-13*	32	46	0.69	0.1243	0.0192	0.5572	0.0865	0.03277	0.00128	450	56	208	8
08GN32.1-14	146	351	0.42	0.0407	0.0049	0.1685	0.0212	0.03005	0.00083	158	18	191	5
08GN32.1-15*	138	377	0.36	0.0368	0.0051	0.1696	0.0246	0.03323	0.00084	159	21	211	5
08GN32.1-16	124	456	0.27	0.0427	0.0049	0.182	0.0219	0.02992	0.00069	170	19	190	4
08GN32.1-17	104	150	0.70	0.0415	0.0071	0.168	0.0279	0.03002	0.00097	158	24	191	6
08GN32.1-18	108	271	0.40	0.0459	0.0052	0.1965	0.0231	0.02985	0.00082	182	20	190	5
08GN32.1-19*	150	205	0.73	0.2409	0.0205	1.1974	0.1046	0.03504	0.00100	799	48	222	6
08GN32.1-20	133	364	0.37	0.0466	0.0050	0.1990	0.0210	0.02991	0.00070	184	18	190	4
08GN32.1-21	166	333	0.50	0.0492	0.0046	0.2047	0.0188	0.03015	0.00059	189	16	191	4
08GN32.1-22	120	257	0.47	0.0634	0.0065	0.2561	0.0269	0.03045	0.00097	232	22	193	6
08GN32.1-23	141	342	0.41	0.0611	0.0057	0.2512	0.0237	0.02988	0.00067	228	19	190	4
08GN32.1-24	228	554	0.41	0.0493	0.0038	0.203	0.017	0.02988	0.00070	188	14	190	4
08GN32.1-25	192	603	0.32	0.0524	0.0038	0.2201	0.0175	0.03002	0.00064	202	15	191	4
08GN36-1													
08GN36.1-1	110	239	0.46	0.0478	0.0050	0.2050	0.0196	0.03050	0.00079	189	17	194	5
08GN36.1-2	172	214	0.80	0.0513	0.0046	0.2225	0.0205	0.03081	0.00071	204	17	196	4
08GN36.1-3	221	311	0.71	0.0466	0.0041	0.1971	0.0169	0.03007	0.00062	183	14	191	4
08GN36.1-4	73	135	0.54	0.0622	0.0065	0.2564	0.0289	0.02912	0.00080	232	23	185	5
08GN36.1-5	107	272	0.39	0.0528	0.0054	0.2200	0.0232	0.02944	0.00060	202	19	187	4
08GN36.1-6	72	155	0.46	0.0571	0.0060	0.2289	0.0236	0.03040	0.00090	209	20	193	6
08GN36.1-7	117	209	0.56	0.0501	0.0057	0.2059	0.0238	0.03018	0.00076	190	20	192	5
08GN36.1-8	86	158	0.54	0.0476	0.0061	0.1901	0.0241	0.02952	0.00078	177	21	188	5
08GN36.1-9	126	192	0.66	0.0499	0.0049	0.2021	0.0191	0.02956	0.00075	187	16	188	5
08GN36.1-10	100	175	0.57	0.0489	0.0062	0.1958	0.0249	0.02948	0.00073	182	21	187	5
08GN36.1-11	118	310	0.38	0.0470	0.0049	0.1968	0.0199	0.02999	0.00069	182	17	190	4
08GN36.1-12*	102	312	0.33	0.0692	0.0043	1.1626	0.0688	0.11763	0.00240	783	32	717	14
08GN36.1-13	97	180	0.54	0.0619	0.0064	0.2544	0.0247	0.02929	0.00068	230	20	186	4
08GN36.1-14*	137	201	0.68	0.1865	0.0133	11.139	0.7300	0.41354	0.00891	2535	61	2231	41
08GN36.1-15	84	141	0.60	0.0564	0.0077	0.2394	0.0312	0.02959	0.00087	218	26	188	5
08GN36.1-16	90	154	0.59	0.0700	0.0084	0.2885	0.0330	0.02912	0.00091	257	26	185	6
08GN36.1-17	54	86	0.64	0.0509	0.0104	0.1973	0.0366	0.03012	0.00104	183	31	191	7
08GN36.1-18*	103	255	0.40	0.0784	0.0048	2.2936	0.1366	0.20429	0.00372	1210	42	1198	20
08GN36.1-19	113	176	0.64	0.0491	0.0058	0.2027	0.0238	0.02962	0.00078	187	20	188	5

(*continued on next page*)

Appendix Table 1 (*continued*)

Analysis	Th	U		Isotopic ratio						Age (Ma)			
	(ppm)	(ppm)	Th/U	$^{207}Pb/^{206}Pb$	$\pm 1\sigma$	$^{207}Pb/^{235}U$	$\pm 1\sigma$	$^{206}Pb/^{238}U$	$\pm 1\sigma$	$^{207}Pb/^{235}U$	$\pm 1\sigma$	$^{206}Pb/^{238}U$	$\pm 1\sigma$
08GN36-1													
08GN36.1-20	96	266	0.36	0.0469	0.0043	0.1929	0.0179	0.02989	0.00074	179	15	190	5
08GN36.1-21	94	175	0.53	0.0435	0.0047	0.1818	0.0215	0.02960	0.00083	170	18	188	5
08GN36.1-22	84	144	0.58	0.0504	0.0063	0.1993	0.0250	0.02923	0.00091	184	21	186	6
08GN36.1-23*	100	164	0.61	0.1670	0.0205	0.9601	0.1540	0.03734	0.00129	683	80	236	8
08GN36.1-24	147	194	0.76	0.0471	0.0055	0.1899	0.0224	0.02991	0.00083	177	19	190	5
08GN36.1-25	70	133	0.53	0.0588	0.0083	0.2417	0.0356	0.02966	0.00087	220	29	188	5

Spots with one and two asterisks are inherited and Pb lost zircon grains, respectively. They are rejected during calculated average age.

Appendix Table 2
Trace elemental analysis results of standard samples and replicate.

Sample	BHVO-2 ($n = 6$)		Recommended value	AGV-2 ($n = 6$)		Recommended value	08GN34-4	08GN34-4
(ppm)		S.D.	By USGS		S.D.	By USGS	replicate	
Sc	31.4	0.33	32	13.2	0.19	13	28.2	28.1
V	315	2.85	317	118	3.63	120	340	358
Cr	282	3.44	280	16.5	0.32	17	84.2	87.1
Mn	1295	16.9	1290	759	11.3	770	1376	1448
Co	44.5	0.55	45	15.8	0.22	16	42.4	43.3
Ni	117	2.73	119	18.7	0.55	19	19.7	27.6
Zn	107	7.95	103	88.8	1.56	86	134	124
Ga	21.2	0.37	21.7	20.7	0.27	20	24.8	22.6
Rb	9.20	0.18	9.8	66.9	1.22	68.6	8.18	8.27
Sr	381	12.1	389	650	8.57	658	309	316
Y	23.3	0.6	26	17.7	0.71	20	35.3	34.5
Zr	171	3.24	172	234	3.95	230	227	246
Nb	17.3	0.18	18	13.2	0.26	15	18.6	17.9
Cs	–	–	–	1.18	0.02	1.16	0.67	0.72
Ba	130	3.94	130	1136	7.29	1140	184	189
La	14.9	0.33	15	37.4	0.73	38	28.2	27.4
Ce	36.9	0.94	38	69.1	1.28	68	59.4	57.6
Pr	5.37	0.13	5.31*	8.34	0.17	8.3	8.07	7.92
Nd	24.9	0.54	25	31.5	0.77	30	34.8	33.2
Sm	6.15	0.1	6.2	5.60	0.08	5.7	7.64	7.48
Eu	2.05	0.03	2.07*	1.52	0.02	1.54	2.41	2.28
Gd	5.89	0.12	6.3	4.71	0.1	4.69	7.41	7.31
Tb	0.94	0.02	0.9	0.64	0.01	0.64	1.20	1.18
Dy	5.23	0.09	5.31*	3.47	0.09	3.6	7.06	6.84
Ho	0.99	0.02	1.04	0.68	0.02	0.71	1.41	1.36
Er	2.43	0.05	2.54*	1.78	0.05	1.79	3.87	3.71
Tm	0.32	0.01	0.34*	0.25	0.01	0.26	0.56	0.54
Yb	1.93	0.05	2	1.60	0.06	1.6	3.47	3.32
Lu	0.28	0.01	0.28	0.25	0.01	0.25	0.53	0.49
Hf	4.56	0.09	4.1	5.39	0.12	5.08	5.75	6.20
Ta	1.16	0.02	1.4	0.84	0.01	0.89	1.28	1.28
Pb	–	–	–	12.8	0.64	13	10.7	12.1
Th	1.22	0.03	1.21	6.17	0.04	6.1	6.73	7.02
U	0.42	0.01	–	1.88	0.01	1.88	1.12	1.18

Data with asterisk are from Raczek et al. (2001).
Reference:
Raczek, I., Stoll, B., Hofmann, A.W., Jochum, K.P. 2001. High-precision trace element data for the USGS reference materials BCR-1, BCR-2, BHVO-1, BHVO-2, AGV-1, AGV-2, DTS-1, DTS-2, GSP-1 and GSP-2 by ID-TIMS and MIC-SSMS. Geostandards Newsletter 25(1), 77–86.

References

Beattie, P., 1993. Olivine-melt and orthopyroxene-melt equilibria. Contributions to Mineralogy and Petrology 115 (1), 103–111.

Bird, P., 1998. Kinematic history of the Laramide orogeny in latitudes 35°–49°N, western United States. Tectonics 17, 780–801.

Black, L.P., Kamo, S.L., Allen, C.M., Aleinikoff, J.N., Davis, D.W., Korsch, R.J., Foudoulis, C., 2003. TEMORA 1: a new zircon standard for Phanerozoic U–Pb geochronology. Chemical Geology 200 (1), 155–170.

Bown, J.W., White, R.S., 1995. Effect of finite extension rate on melt generation at rifted continental margins. Journal of Geophysical Research: Solid Earth 100 (B9), 18011–18029.

Carter, A., Roques, D., Bristow, C., Kinny, P., 2001. Understanding Mesozoic accretion in Southeast Asia: significance of Triassic thermotectonism (Indosinian orogeny) in Vietnam. Geology 29, 211–214.

Chen, P.R., Kong, X.G., Ni, Q.S., Zhang, B.T., Liu, C.S., 1999a. Ascertainment and implication of the Early Yianshanian bimaodal volcanic associations from south Jiangxi Province. Geological Review 45, 734–741 (in Chinese).

Chen, P.R., Kong, X.G., Wang, Y.X., Ni, Q.S., Zhang, B.T., Liu, H.F., 1999b. Rb-Sr isotopic dating and significance of Early Yanshanian bimodal vocalnic-intrusive. Geological Journal of China Universities 5 (4), 378–383 (in Chinese).

Chen, P.R., Zhou, X.M., Zhang, W.L., Li, H.M., Fan, C.F., Sun, T., Chen, W.F., Zhang, M., 2004. Petrogenesis of eastern Nanning Early Yanshanian synites and granitic complex and its implication. Science in China: Earth Science 34 (6), 493–503 (in Chinese).

Coney, P.J., Reynolds, S.J., 1977. Cordilleran Benioff zones. Nature 270, 403–406.

Cui, S., Li, J., 1983. On the Indosinian Orogeny along the Chinese western Pacific belt. Acta Geologica Sinica 51–61 (in Chinese).

Dasgupta, R., Hirschmann, M.M., Stalker, K., 2006. Immiscible transition from carbonate-rich to silicate-rich melts in the 3 GPa melting interval of eclogite + CO_2 and genesis of silica-undersaturated ocean island lavas. Journal of Petrology 47 (4), 647–671.

Dasgupta, R., Hirschmann, M.M., Smith, N.D., 2007. Partial melting experiments of peridotite + CO_2 at 3 GPa and genesis of alkalic ocean island basalts. Journal of Petrology 48 (11), 2093–2124.

Dickinson, W.R., Snyder, W.S., 1978. Plate tectonics of the Laramide Orogeny. In: Matthews, V. (Ed.), Laramide folding associated with basement block faulting in the western United States. Geological Society of America Memoir 151, pp. 355–366.

Dixon, J.E., Leist, L., Langmuir, C., Schilling, J.G., 2002. Recycled dehydrated lithosphere observed in plume-influenced mid-ocean-ridge basalt. Nature 420 (6914), 385–389.
Dong, C.Y., Zhao, K.D., Jiang, S.Y., Chen, W.F., 2010. Zircon geochronology, geochemistry and petrogenesis of granite from the Baimianshi uranium ore district in the southern Jiangxi Province. Geological Journal of China Universities 16 (2), 149–160 (in Chinese).
Ellam, R.M., 1992. Lithospheric thickness as a control on basalt geochemistry. Geology 20 (2), 153–156.
Falloon, T.J., Danyushevsky, L.V., 2000. Melting of refractory mantle at 1.5, 2 and 2.5 GPa under anhydrous and H_2O-undersaturated conditions: implications for the petrogenesis of high-Ca boninites and the influence of subduction components on mantle melting. Journal of Petrology 41 (2), 257–283.
Fang, W.X., Hu, R.Z., Su, W.C., Xiao, R.F., Qi, L., Jiang, G.H., 2002. Emplacement age of Zhenyuan lamproite in Guizhou. China Science Bulletin 47, 307–312 (in Chinese with English abstract).
Ferguson, D.J., Maclennan, J., Bastow, I.D., Pyle, D.M., Jones, S.M., Keir, D., Blundy, J.D., Plank, T., Yirgu, G., 2013. Melting during late-stage rifting in Afar is hot and deep. Nature 499 (7456), 70–73.
Green, D.H., Ringwood, A.E., 1963. Mineral assemblages in a model mantle composition. Journal of Geophysical Research 68 (3), 937–945.
He, Z.Y., Xu, X.S., Chen, R., Xing, G.F., 2007. Genesis of Middle Jurassic syenite-gabbro in southern Jiangxi Province and their geological significance. Acta Petrologica Sinica 23, 1457–1469 (in Chinese with English abstract).
He, Z.Y., Xu, X.S., Niu, Y., 2010. Petrogenesis and tectonic significance of a Mesozoic granite–syenite–gabbro association from inland South China. Lithos 119 (3–4), 621–641.
Heinonen, J.S., Luttinen, A.V., Riley, T.R., Michallik, R.M., 2013. Mixed pyroxenite-peridotite sources for mafic and ultramafic dikes from the Antarctic segment of the Karoo continental flood basalt province. Lithos 177, 366–380.
Herzberg, C., 2011. Identification of source lithology in the Hawaiian and Canary Islands: implications for origins. Journal of Petrology 52 (1), 113–146.
Herzberg, C., Asimow, P.D., 2008. Petrology of some oceanic island basalts: PRIMELT2.XLS software for primary magma calculation. Geochemistry, Geophysics, Geosystems 9 (9), 1–25.
Herzberg, C., O'Hara, M.J., 2002. Plume-associated ultramafic magmas of phanerozoic age. Journal of Petrology 43 (10), 1857–1883.
Herzberg, C., Asimow, P.D., Arndt, N., Niu, Y., Lesher, C.M., Fitton, J.G., Cheadle, M.J., 2007. Temperatures in ambient mantle and plumes: constraints from basalts, picrites, and komatiites. Geochemistry, Geophysics, Geosystems 8 (2), 1–34.
Hirose, K., Kushiro, I., 1993. Partial melting of dry peridotites at high pressures: determination of compositions of melts segregated from peridotite using aggregates of diamond. Earth and Planetary Science Letters 114 (4), 477–489.
Hirschmann, M.M., Kogiso, T., Baker, M.B., Stolper, E.M., 2003. Alkalic magmas generated by partial melting of garnet pyroxenite. Geology 31 (6), 481–484.
Hsieh, P.S., Chen, C.H., Yang, H.J., Lee, C.Y., 2008. Petrogenesis of the Nanling Mountains granites from South China: constraints from systematic apatite geochemistry and whole-rock geochemical and Sr–Nd isotope compositions. Journal of Asian Earth Sciences 33 (5), 428–451.
Jahn, B.M., Zhou, X.H., Li, J.L., 1990. Formation and tectonic evolution of Southeastern China and Taiwan: isotopic and geochemical constraints. Tectonophysics 183, 145–160.
Ji, C.Y., Wu, J.H., 2010. The SHRIMP zircon U–Pb dating of felsic volcanic rocks and its geological significance from Yutian group in southern Jiangxi. Journal of East China Institute of Technology 33 (02), 131–138 (in Chinese).
Jiang, Y.H., Ling, H.F., Jiang, S.Y., Fan, H.H., Shen, W.Z., Ni, P., 2005. Petrogenesis of a Late Jurassic peraluminous volcanic complex and its high-Mg, potassic, quenched enclaves at Xiangshan, Southeast China. Journal of Petrology 46 (6), 1121–1154.
Jung, S., Vieten, K., Romer, R.L., Mezger, K., Hoernes, S., Satir, M., 2012. Petrogenesis of tertiary alkaline magmas in the Siebengebirge, Germany. Journal of Petrology 53, 2381–2409.
Katz, R.F., Spiegelman, M., Langmuir, C.H., 2003. A new parameterization of hydrous mantle melting. Geochemistry, Geophysics, Geosystems 4 (9), 1–19.
Kelley, K.A., Plank, T., Grove, T.L., Stolper, E.M., Newman, S., Hauri, E., 2006. Mantle melting as a function of water content beneath back-arc basins. Journal of Geophysical Research 111 (B9), 1–27.
Klein, E.M., Langmuir, C.H., 1987. Global correlations of ocean ridge basalt chemistry with axial depth and crustal thickness. Journal of Geophysical Research 92 (B8), 8089–8115.
Langmuir, C.H., Klein, E.M., Plank, T., 1992. Petrological systematics of mid-ocean ridge basalts: constraints on melt generation beneath ocean ridges. Mantle Flow and Melt Generation at Mid-Ocean Ridges, American Geophysical Union, Geophysical Monograph 71, 183–280.
Le Roux, V., Lee, C.T.A., Turner, S.J., 2010. Zn/Fe systematics in mafic and ultramafic systems: implications for detecting major element heterogeneities in the Earth's mantle. Geochimica et Cosmochimica Acta 74 (9), 2779–2796.
Lee, C.T.A., Luffi, P., Plank, T., Dalton, H., Leeman, W.P., 2009. Constraints on the depths and temperatures of basaltic magma generation on Earth and other terrestrial planets using new thermobarometers for mafic magmas. Earth and Planetary Science Letters 279 (1-2), 20–33.
Li, Z.X., Li, X.H., 2007. Formation of the 1300-km-wide intracontinental orogen and postorogenic magmatic province in Mesozoic South China: a flat-slab subduction model. Geology 35 (2), 179–182.
Li, X.H., Chen, Z.G., Liu, D.Y., Li, W.X., 2003. Jurassic gabbro-granite-syenite suites from southern Jiangxi Province, SE China: age, origin, and tectonic significance. International Geology Review 45 (10), 898–921.
Li, X.H., Chung, S.L., Zhou, H.W., Lo, C.H., Liu, Y., Chen, C.H., 2004. Jurassic intraplate magmatism in southern Hunan–eastern Guangxi: 40Ar/39Ar dating, geochemistry, Sr–Nd isotopes and implications for the tectonic evolution of SE China. Geological Society, London, Special Publications 226 (1), 193–215.
Li, X.H., Li, Z.X., Wingate, M.T.D., Chung, S.L., Liu, Y., Lin, G.C., Li, W.X., 2006. Geochemistry of the 755 Ma Mundine Well dyke swarm, Northwestern Australia: part of a Neoproterozoic mantle superplume beneath Rodinia? Precambrian Research 146 (1), 1–15.
Li, X.H., Li, W.X., Wang, X.C., Li, Q.L., Liu, Y., Tang, G.Q., Gao, Y.Y., Wu, F.Y., 2010. SIMS U–Pb zircon geochronology of porphyry Cu-Au-(Mo) deposits in the Yangtze River Metallogenic Belt, eastern China: magmatic response to Early Cretaceous lithospheric extension. Lithos 119, 427–438.
Li, Z.X., Li, X.H., Chung, C.L., Lo, C.H., Xu, X.S., Li, W.X., 2012a. Magmatic switch-on and switch-off along the South China continental margin since the Permian: transition from an Andean-type to a Western Pacific-type plate boundary. Tectonophysics 532-535, 271–290.
Li, X.H., Li, Z.X., He, B., Li, W.X., Li, Q.L., Gao, Y., Wang, X.C., 2012b. The Early Permian active continental margin and crustal growth of the Cathaysia Block: in situ U–Pb, Lu–Hf and O isotope analyses of detrital zircons. Chemical Geology 328, 195–207.
Li, X.W., Mo, X.X., Yu, X.H., Ding, Y., Huang, X.W., Wei, P., He, W.Y., 2013. Geochronological, geochemical and Sr–Nd–Hf isotopic constraints on the origin of the Cretaceous intraplate volcanism in West Qinling, Central China: implications for asthenosphere–lithosphere interaction. Lithos 117, 381–401.
Liu, Y.S., Hu, Z.C., Gao, S., Gunther, D., Xu, J., Gao, C.G., Chen, H.H., 2008. In situ analysis of major and trace elements of anhydrous minerals by LA–ICP–MS without applying an internal standard. Chemical Geology 257 (1), 34–43.
Mckenzie, D., Bickle, M.J., 1988. The volume and composition of melt generated by extension of the lithosphere. Journal of Petrology 29 (3), 625–679.
Mckenzie, D., O'Nions, R.K., 1991. Partial melt distributions from inversion of rare earth element concentrations. Journal of Petrology 32, 1021–1091.
Michael, P., 1995. Regionally distinctive sources of depleted MORB: evidence from trace elements and H_2O. Earth and Planetary Science Letters 131 (3), 301–320.
O'Hara, M.J., 1967. Mineral facies in ultrabasic rocks. In: Wyllie, P.J. (Ed.), Ultramafic and related rocks, pp. 7–18.
Pang, C.J., Krapez, B., Li, Z.X., Xu, Y.G., Liu, H.Q., Cao, J., 2014. Stratigraphic evolution of a Late Triassic to Early Jurassic intracontinental basin in southeastern South China: a consequence of flat-slab subduction. Sedimentary Geology 302, 44–63.
Pilet, S., Baker, M.B., Stolper, E.M., 2008. Metasomatized lithosphere and the origin of alkaline lavas. Science 320 (5878), 916–919.
Polat, A., Hofmann, A.W., Rosing, M.T., 2002. Boninite-like volcanic rocks in the 3.7–3.8 Ga Isua greenstone belt, West Greenland: geochemical evidence for intra-oceanic subduction zone processes in the early Earth. Chemical Geology 184 (3-4), 231–254.
Roeder, P.L., Emslie, R.F., 1970. Olivine-liquid equilibrium. Contributions to Mineralogy and Petrology 29 (4), 275–289.
Sobolev, A.V., Hofmann, A.W., Sobolev, S.V., Nikogosian, I.K., 2005. An olivine-free mantle source of Hawaiian shield basalts. Nature 434 (7033), 590–597.
Sobolev, A.V., Hofmann, A.W., Kuzmin, D.V., Yaxley, G.M., Arndt, N.T., Chung, S.L., Danyushevsky, L.V., Elliott, T., Frey, F.A., Garcia, M.O., 2007. The amount of recycled crust in sources of mantle-derived melts. Science 316 (5823), 412–417.
Sun, S.S., McDonough, W.F., 1989. Chemical and isotopic systematics of oceanic basalts: implications for mantle composition and processes. Geological Society, London, Special Publications 42 (1), 313–345.
Tanaka, T., Togashi, S., Kamioka, H., Amakawa, H., Kagami, H., Hamamoto, T., Yuhara, M., Orihashi, Y., Yoneda, S., Shimizu, H., 2000. JNdi-1: a neodymium isotopic reference in consistency with La Jolla neodymium. Chemical Geology 168 (3), 279–281.
Tao, J.H., Li, W.X., Li, X.H., Cen, T., 2013. Petrogenesis of early Yanshanian highly evolved granites in the Longyuanba area, southern Jiangxi Province: evidence from zircon U–Pb dating, Hf–O isotope and whole-rock geochemistry. Science China: Earth Sciences 56 (6), 922–939.
Tschegg, C., Ntaflos, T., Akinin, V.V., 2011. Polybaric petrogenesis of Neogene alkaline magmas in an extensional tectonic environment: Viliga Volcanic Field, northeast Russia. Lithos 122, 13–24.
Wang, K., Plank, T., Walker, J.D., Smith, E.I., 2002. A mantle melting profile across the Basin and Range, SW USA. Journal of Geophysical Research 107, 1–21.
Wang, Y.J., Fan, W.M., Guo, F., Peng, T.P., Li, C.W., 2003. Geochemistry of Mesozoic mafic rocks adjacent to the Chenzhou–Linwu fault, South China: implications for the lithospheric boundary between the Yangtze and Cathaysia blocks. International Geological Review 45, 263–286.
Wang, Y.J., Fan, W.M., Peng, T.P., Guo, F., 2005. Elemental and Sr–Nd isotopic systematics of the early Mesozoic volcanic sequence in southern Jiangxi Province, South China: petrogenesis and tectonic implications. International Journal of Earth Sciences 94 (1), 53–65.
Wang, Y.J., Fan, W.M., Sun, M., Liang, X.Q., Zhang, Y.H., Peng, T.P., 2007a. Geochronological, geochemical and geothermal constraints on petrogenesis of the Indosinian peraluminous granites in the South China Block: a case study in the Hunan Province. Lithos 96 (3), 475–502.
Wang, X.C., Li, X.H., Li, W.X., Li, Z.X., 2007b. Ca. 825 Ma komatiitic basalts in South China: first evidence for >1500°C mantle melts by a Rodinian mantle plume. Geology 35 (12), 1103–1106.
Wang, X.C., Li, X.H., Li, W.X., Li, Z.X., Liu, Y., Yang, Y.H., Liang, X.R., Tu, X.L., 2008. The Bikou basalts in the northwestern Yangtze block, South China: Remnants of 820–810 Ma continental flood basalts? Geological Society of America Bulletin 120 (11-12), 1478–1492.
Wang, X.C., Li, X.H., Li, W.X., Li, Z.X., 2009. Variable involvements of mantle plumes in the genesis of mid-Neoproterozoic basaltic rocks in South China: a review. Gondwana Research 15 (3-4), 381–395.

Wang, X.C., Li, X.H., Li, Z.X., Liu, Y., Yang, Y.H., 2010. The Willouran basic province of South Australia: its relation to the Guibei large igneous province in South China and the breakup of Rodinia. Lithos 119 (3-4), 569–584.
Wang, X.C., Li, Z.X., Li, X.H., Li, J., Liu, Y., Long, W.G., Zhou, J.B., Wang, F., 2012. Temperature, pressure, and composition of the mantle source region of Late Cenozoic basalts in Hainan Island, SE Asia: a consequence of a young thermal mantle plume close to subduction zones? Journal of Petrology 53 (1), 177–233.
Wang, Y.J., Fan, W.M., Zhang, G.W., Zhang, Y.H., 2013. Phanerozoic tectonics of the South China block: key observations and controversies. Gondwana Research 23 (4), 1273–1305.
Wang, X.C., Li, Z.X., Li, J., Pisarevsky, S.A., Wingate, M.T., 2014. Genesis of the 1.21 Ga Marnda Moorn large igneous province by plume–lithosphere interaction. Precambrian Research 241, 85–103.
Wang, X.C., Wilde, S.A., Li, Q.L., Yang, Y.N., 2015. Continental flood basalts derived from the hydrous mantle transition zone. Nature Communications 6, 7700.
Wang, X.C., Wilde, S.A., Xu, B., Pang, C.J., 2016. Origin of arc-like continental basalts: Implications for deep-Earth fluid cycling and tectonic discrimination. Lithos, http://dx.doi.org/10.1016/j.lithos.2015.12.014 (in press).
White, R., McKenzie, D., 1989. Magmatism at rift zones: the generation of volcanic continental margins and flood basalts. Journal of Geophysical Research 94 (B6), 7685–7729.
White, R.S., McKenzie, D., 1995. Mantle plumes and flood basalts. Journal of Geophysical Research 100, 17543–17585.
Wilson, M., 1989. Igneous Petrogenesis. Chapman and Hall.
Winchester, J., Floyd, P., 1976. Geochemical magma type discrimination: application to altered and metamorphosed basic igneous rocks. Earth and Planetary Science Letters 28 (3), 459–469.
Wu, J.H., Zhou, W.X., Zhang, B.T., 2000. Stratigraphic division and geologic era of mesozoic era volcanic rock series in South Jiangxi–North Guangdong. Geological Review 46 (4), 362–370 (in Chinese).
Wu, F.Y., Yang, Y.H., Xie, L.W., Yang, J.H., Xu, P., 2006. Hf isotopic compositions of the standard zircons and baddeleyites used in U–Pb geochronology. Chemical Geology 234, 105–126.
Xiang, Y.X., Wu, J.H., 2012. SHRIMP zircon U–Pb age of Yutian Group basalts in Longnan area of southern Jiangxi Province and its geological significance. Geological Bulletin of China 31 (05), 716–725 (in Chinese).
Xie, G.Q., Hu, R.Z., Zhao, J.H., Jiang, G.H., 2001. Mantle plume and the relationship between it and mesozoic large-scale metallogenesis in southeastern China: a preliminary discussion. Geotectonica et Metallogenia 25 (2), 179–186 (in Chinese).
Xu, M.H., 1992. Early Jurassic bimodal volcanic rocks and their structure environment in Yongding County, Fujian Province. Geology of Fujian 11, 115–125.
Xu, Y.G., Chung, C.L., Jahn, B.M., Wu, G.Y., 2001. Petrologic and geochemical constraints on the petrogenesis of Permian–Triassic Emeishan flood basalts in southwestern China. Lithos 58, 145–168.
Xu, Y.G., Zhang, H.H., Qiu, H.N., Ge, W.C., Wu, F.Y., 2012. Oceanic crust components in continental basalts from Shuangliao, Northeast China: derived from the mantle transition zone? Chemical Geology 328, 168–184.
Yu, X.Q., Wu, G.G., Zhao, X.X., Gao, J.F., Di, Y.J., Zheng, Y., Dai, Y.P., Li, C.L., Qiu, J.T., 2010. The Early Jurassic tectono-magmatic events in southern Jiangxi and northern Guangdong provinces, SE China: constraints from the SHRIMP zircon U–Pb dating. Journal of Asian Earth Sciences 39 (5), 408–422.
Zhang, Z.J., Badal, J., Li, Y.K., Chen, Y., Yang, L.Q., Teng, J.W., 2005. Crust-upper mantle seismic velocity structure across Southeastern China. Tectonophysics 395, 137–157.
Zhang, Y.Y., Yuan, C., Sun, M., Long, X.P., Xia, X.P., Wang, X.Y., Huang, Z.Y., 2015. Permian doleritic dikes in the Beishan Orogenic Belt, NW China: asthenosphere–lithosphere interaction in response to slab break-off. Lithos 233, 174–192.
Zhou, J.C., Chen, R., 2001. Geochemistry of Late Mesozoic interaction between crust and mantle in southeastern Fujian Province. Geochimica 30 (6), 547–558.
Zhou, X.M., Li, W.X., 2000. Origin of Late Mesozoic igneous rocks in Southeastern China: implications for lithosphere subduction and underplating of mafic magmas. Tectonophysics 326 (3), 269–287.
Zhou, J.C., Jiang, S.Y., Wang, X.L., Yang, J.H., Zhang, M.Q., 2005a. Re–Os isochron age of Fankeng basalts from Fujian of SE China and its geological significance. Geochemical Journal 39, 497–502.
Zhou, J.C., Jiang, S.Y., Wang, X.L., Yang, J.H., Zhang, M.Q., 2005b. Geochemical study of Middile Jurrasic basalts in South China: a case study from Fankeng, Fujian Province. Science in China: Earth Science 35 (10), 927–936 (in Chinese).
Zhou, X.M., Sun, T., Shen, W.Z., Shu, L.S., Niu, Y., 2006. Petrogenesis of Mesozoic granitoids and volcanic rocks in South China: a response to tectonic evolution. Episodes 29 (1), 26–33.
Zhu, W.G., Zhong, H., Li, X.H., He, D.F., Song, X.Y., Ren, T., Chen, Z.Q., Sun, H.S., Liao, J.Q., 2010. The Early Jurassic mafic–ultramafic intrusion and A-type granite from northeastern Guangdong, SE China: age, origin, and tectonic significance. Lithos 119 (3-4), 313–329.